Karlsruhe Institute of Technology

Institute for Theoretical Physics

Dark Matter Generation Mechanisms of the Model „CP In The Dark“

Master’s Thesis of

Johann Plotnikov

at the Department of Physics
Institute for Theoretical Physics (ITP)

Reviewer:	Prof. Dr. Milada Margarete Mühlleitner
Second reviewer:	PD Dr. Stefan Gieseke
Advisor:	Dr. Duarte Azevedo

01. April 2022 – 23. March 2023

I declare that I have developed and written the enclosed thesis completely by myself, and have not used sources or means without declaration in the text.

Karlsruhe, 23.03.2023

. . . .

(Johann Plotnikov)

Accepted as Master thesis.

Karlsruhe, 23.03.2023

. . . .

(Prof. Dr. M. M. Mühlleitner)

Contents

List of Figures

List of Tables

1. Introduction

With the discovery of the Higgs boson in 2012 by the Large Hadron Collider experiments ATLAS [1] and CMS [2], the Standard Model (SM) of particle physics was completed. Even though the SM explains the today known fundamental building blocks of matter and the fundamental forces that act between them (with the exception of gravity), there are still some problems which it cannot solve. Problems such as the hierarchy problem, the baryon asymmetry of the universe and the observed Dark Matter (DM) relic density cannot be explained by the SM.

The hierarchy problem addresses the question why the mass of the Higgs boson is of the order of the electroweak scale even in the presence of large energy scales, like the Planck scale up to which the SM can in principle be valid. In the SM it can be shown that corrections to the mass of the Higgs boson at $m_h = 125.09\,\text{GeV}$ [3] are quadratic with respect to the energy scale and can therefore give large contributions to its mass, if the SM is valid up to the Planck scale. Although this problem can be solved by fine tuning the SM parameters, it shifts the problem to the question why such a fine tuning of parameters is necessary in the first place and if there is a more natural way to keep the mass low at high energy scales, given e.g. by symmetry arguments. A prominent SM extension that solves the hierarchy problem is e.g. given by supersymmetry (For reviews and introduction, see e.g. [4, 5]), a symmetry between fermions and bosons, where each SM particle has a supersymmetric counterpart particle which differs by half unit in spin.

The observed baryon asymmetry of the universe (BAU) asks the question as to why there is more matter than antimatter in the universe. If matter and antimatter were in thermal equilibrium at the beginning of the universe why is there now more matter than antimatter [6]. The value of the currently observed BAU is given by the PLANCK collaboration at [7]

$$\eta = \frac{n_b - n_{\bar{b}}}{n_\gamma} = 6.1 \cdot 10^{-10} \quad . \tag{1.1}$$

This baryon asymmetry can be generated dynamically through electroweak baryogenesis (EWBG), provided the three Sakharov conditions [8] are fulfilled. These are

- baryon number violating processes,
- charge (C) and charge-parity (CP) symmetry violation and
- interactions out of thermal equilibrium.

Even though the SM allows for C and CP violating processes, the CP violation is not large enough to explain the currently observed BAU measured by PLANCK. Further, to fulfill the third Sakharov condition, a departure from thermal equilibrium is required. In the case of EWBG this departure from thermal equilibrium can only be caused by a strong first order electroweak phase transition (SFOEWPT) [9]. To enable an SFOEWPT in the SM, the Higgs boson would need to have a mass between 70-80 GeV [10, 11], which is in disagreement with the current measurement. Therefore, if the BAU is generated via the mechanism of electroweak symmetry breaking there is a need for beyond-the-SM (BSM) physics.

Numerous astrophysical and cosmological observations point towards the existence of matter that is not directly visible but interacts gravitationally. Phenomena such as the rotation curves of stars in galaxies [12–14], gravitational lensing effects of the bullet cluster [15] and temperature variations in the Cosmic Microwave Background (CMB) can be explained by the existence of DM.

In this thesis the open question for the nature of DM is investigated. For this, a model called *CP in the Dark* [16] will be investigated. This model introduces an extension of the scalar sector of the SM with two complex scalar doublets and a real scalar singlet. Not only does it provide a stable DM candidate but also adds novel additional CP violation in the dark sector necessary for the generation of the BAU through EWBG. The upside of having the additional CP violation purely in the dark sector is that constraints from the electric dipole moment do not need to be considered [17, 18]. The parameter space of *CP in the Dark* has already been thoroughly analyzed in the case where the DM abundance is generated thermally via the mechanism called freeze-out [16]. In this mechanism the DM particles start in thermal equilibrium with the SM particle bath at the beginning of the universe. At some point during the expansion and therefore cooling down of the universe, the DM particles decouple from the SM bath and through DM pair annihilations are able to lead to today's observed relic density measured by PLANCK [7]

$$\Omega_{\text{obs}}h^2 = 0.120 \pm 0.001 \quad . \tag{1.2}$$

However, when only considering freeze-out the number of parameter points that can fully account for the observed relic density, while simultaneously fulfilling the most relevant theoretical and experimental constraints, is limited. The goal of this thesis is to introduce a second mechanism which is able to produce DM thermally into *CP in the Dark*, called freeze-in. In freeze-in the DM particles are not in thermal equilibrium with the SM, but instead start with no initial abundance. The DM particles get produced either via the decays of SM particles or through SM pair annihilations. This allows to fill the gap between the relic density generated via freeze-out and the experimental value given in Eq. (1.2).

The main part of this thesis is the development of a code that is able to calculate the relic density generated via freeze-in for *CP in the Dark*. For the relic density generated via freeze-out, the code `MicrOMEGAs` [19] will be used. Further, the conditions necessary to create a scenario in *CP in the Dark* in which both mechanisms (freeze-out and freeze-in) contribute to the same relic density will be determined. A scan of the parameter region in which both mechanisms are possible will be done and its phenomenological implications will be investigated. In this scan the same constraints as in the original paper [16] will be applied with updated experimental data. This will be done using the code `ScannerS` [20, 21] and the code developed in this thesis.

The structure of this thesis will be as follows. In Chapter 2, the theoretical foundation of this thesis will be established. Section 2.1 introduces the SM and Sec. 2.2 the model *CP in the Dark*. The main evidences for DM and how it can be searched for will be discussed in Secs. 2.3 and 2.4, respectively. Chapter 3 will set up the mathematical and phenomenological framework to understand thermal DM production via freeze-out and freeze-in. In this framework, Chapter 4 will show the possibility of freeze-in in *CP in the Dark*. Chapter 5 lists and discusses the relevant experimental and theoretical constraints taken into account to generate a viable set of parameter points for the numerical analysis. In Chapter 6 a detailed description of the developed code to calculate the relic density generated via freeze-in will be given. The results of this thesis will be presented in Chapter 7. Conclusions are given in Chapter 8.

2. Theoretical Background

Section 2.1 will establish the terminology and notation used to describe models in particles physics by giving a short summary of the SM. In Sec. 2.2 the introduction of *CP in the Dark* will be done. The three main evidences for DM will be presented in Sec. 2.3. Possible methods of detecting DM will be discussed on Sec. 2.4.

2.1. The Standard Model of Particle Physics

The SM is currently the best description of all the discovered fundamental particles and forces except gravity. These forces are the strong interaction, the weak interaction and the electromagnetic interaction and are associated with the local invariance of the gauge groups $SU(3)_C$, $SU(2)_L$ and $U(1)_Y$ [22].

The theoretical framework used to describe the SM is quantum field theory in which excitations of these fields represent particles. Local gauge invariance of the gauge groups introduces gauge fields into the SM, whose excitations result in gauge bosons which are the mediators of the above mentioned interactions.

Gluons G^a_μ, that result from the local invariance of $SU(3)_C$ mediate the strong interaction. The gauge bosons B^μ and $W^\mu_{1,2,3}$, resulting from the $SU(2)_L \times U(1)_Y$ groups, represent the mediators of the electroweak interaction.

All particles carry quantum numbers and have specific transformation properties under the gauge groups that determine how they interact with each other through gauge bosons. The fermions consisting of six quarks and six leptons have non-zero isospin and hypercharge quantum numbers and are therefore subject to the electroweak force. However, the former also carry a colour charge and thus, can interact via the strong force.

To maintain the chiral symmetries, the Lagrangian of the SM does not allow an inclusion of bilinear mass terms for neither fermions nor gauge bosons. In order to avoid that, Brout, Engler and Higgs proposed a mechanism that gives masses to these particles without violating the symmetries of the SM [23, 24].

The so called Higgs mechanism introduces a complex doublet field Φ which is invariant under $SU(2)_L \times U(1)_Y$. This field has a potential $V(\Phi)$ of the form

$$V(\Phi) = \mu^2 \Phi\Phi^\dagger + \lambda(\Phi\Phi^\dagger)^2 \quad , \tag{2.1}$$

with $\mu^2 < 0$. Minimizing the potential with

$$\frac{\partial V}{\partial \Phi} \overset{!}{=} 0 \tag{2.2}$$

leads to the Vacuum Expectation Value (VEV) given by

$$v = \sqrt{\frac{-\mu^2}{\lambda}} \approx 246.22\,\text{GeV} \quad . \tag{2.3}$$

The ground state with non-zero VEV spontaneously breaks the $SU(2)_L \times U(1)_Y$ symmetry down to the electromagnetic $U(1)_{em}$ whose gauge boson is the mediator of the electromagnetic force - the photon A^μ.

Furthermore, the Goldstone theorem [25] states that the difference between the dimension of the symmetry before and after being broken gives the number of generated massless pseudo Goldstone bosons. In the case of the SM, the number is 4-1=3, namely G^0 and $G^\pm$. These bosons appear as degrees of freedom in the theory. In the physical unitary gauge, however, they get absorbed into the mass eigenstates of to the weak gauge bosons $W^\pm$ and Z giving rise to their respective longitudinal modes.

After spontaneous symmetry breaking (SSB), the Higgs boson gives mass to the fermions through the Yukawa sector

$$\mathcal{L}_{Yukawa} = -\overline{L}_L Y_l \Phi l_R - \overline{Q}_L Y_d \Phi d_R - \overline{\tilde{Q}}_L Y_u \Phi u_R + h.c. \quad . \tag{2.4}$$

Here, L_L (Q_L) are the left-handed lepton (quark) doublets, l_R the right-handed leptons, u_R (d_R) the right-handed up-type (down-type) quarks and $Y_{l,d,u}$ are general complex 3×3 matrices.

2.2. CP in the Dark

The model *CP in the Dark* not only introduces a DM candidate but also additional CP violation to accommodate for the observed BAU. It is the minimal model to achieve this via an extension of the scalar sector of the SM with the complex $SU(2)_L$ doublets Φ_1 and Φ_2 and a real singlet scalar field Φ_s [16]. Moreover, it imposes a $\mathbb{Z}_2$ symmetry on its fields in the form of

$$\Phi_1 \to \Phi_1 \ , \ \ \Phi_2 \to -\Phi_2 \ , \ \ \Phi_s \to -\Phi_s \quad . \tag{2.5}$$

With this symmetry the most general scalar potential invariant under $SU(2)_L \times U(1)_Y$ reads

$$\begin{aligned} V =& m_{11}^2|\Phi_1|^2 + m_{22}^2|\Phi_2|^2 + \frac{1}{2}m_S^2\Phi_S^2 + \left(A\Phi_1^\dagger\Phi_2\Phi_S + h.c.\right) \\ &+ \frac{1}{2}\lambda_1|\Phi_1|^4 + \frac{1}{2}\lambda_2|\Phi_2|^4 + \lambda_3|\Phi_1|^2|\Phi_2|^2 + \lambda_4|\Phi_1^\dagger\Phi_2|^2 \\ &+ \frac{1}{2}\lambda_5\left[\left(\Phi_1^\dagger\Phi_2\right)^2 + h.c.\right] + \frac{1}{4}\lambda_6\Phi_S^4 + \frac{1}{2}\lambda_7|\Phi_1|^2\Phi_S^2 + \frac{1}{2}\lambda_8|\Phi_2|^2\Phi_S^2 \quad . \end{aligned} \tag{2.6}$$

The parameters m_{11}, m_{22}, m_S, λ_{1-4} and λ_{6-8} are real due to the hermicity of the potential. The couplings λ_5 and A are complex in general. However, here the basis freedom to redefine doublets is used to absorb the complex phase of λ_5 to make it real.

All fermion fields are considered neutral under the $\mathbb{Z}_2$ symmetry. As a result of that only Φ_1 couples to fermions in an identical way as the SM doublet Φ in Eq. (2.4). This ensures that no tree-level, flavour-changing currents (FCNC) are allowed. Consider now SSB in which only Φ_1 acquires a non-zero VEV,

$$\langle \Phi_1 \rangle = \begin{pmatrix} 0 \\ \frac{v}{\sqrt{2}} \end{pmatrix} \quad , \tag{2.7}$$

where the brackets denote the vacuum state of Φ_1. Because all fermion and gauge boson masses are generated by Φ_1 the value of v has to be equal to the SM one in Eq. (2.3). From the minimisation conditions

$$\left.\frac{\partial V}{\partial \Phi_a}\right|_{\Phi_i = \langle \Phi_i \rangle} = 0 \ , \quad a, i \in \{1, 2, S\} \quad , \tag{2.8}$$

it follows that

$$m_{11}^2 + \frac{1}{2}\lambda_1 v^2 = 0 \quad . \tag{2.9}$$

After electroweak symmetry breaking the doublets can be written in terms of their component fields as

$$\Phi_1 = \begin{pmatrix} G^+ \\ \frac{1}{\sqrt{2}}\left(v + h + iG^0\right) \end{pmatrix} \ , \ \Phi_2 = \begin{pmatrix} H^+ \\ \frac{1}{\sqrt{2}}(\rho + i\eta) \end{pmatrix} \quad . \tag{2.10}$$

Here h is the SM-like Higgs boson, G^+ and G^0 the charged and neutral Goldstone bosons and H^+ the charged scalar. These are mass eigenstates with the masses given by

$$\begin{aligned} m_h^2 =& \lambda_1 v^2 \quad , \\ m_{G^+}^2 =& m_{G^0}^2 = 0 \quad \text{and} \\ m_{H^+}^2 =& m_{22}^2 + \frac{1}{2}\lambda_3 v^2 \quad . \end{aligned} \tag{2.11}$$

Since the value of the Higgs mass is measured to be $m_h = 125.09\,\mathrm{GeV}$ [26, 27], Eq. (2.9) fixes the quartic coupling to $\lambda_1 \approx 0.258$. The other neutral fields ρ and η mix with the singlet Φ_s to generate the mass eigenstates h_1, h_2 and h_3 by the rotation matrix R

$$\begin{pmatrix} h_1 \\ h_2 \\ h_3 \end{pmatrix} = R \begin{pmatrix} \rho \\ \eta \\ \Phi_s \end{pmatrix} \quad . \tag{2.12}$$

This orthogonal matrix is parameterized by the angles α_1, α_2 and α_3 with $\alpha_i \in \left[-\frac{\pi}{2}, \frac{\pi}{2}\right]$ so that

$$R = \begin{pmatrix} c_{\alpha_1} c_{\alpha_2} & s_{\alpha_1} c_{\alpha_2} & s_{\alpha_2} \\ -(c_{\alpha_1} s_{\alpha_2} s_{\alpha_3} + s_{\alpha_1} c_{\alpha_3}) & c_{\alpha_1} c_{\alpha_3} - s_{\alpha_1} s_{\alpha_2} s_{\alpha_3} & c_{\alpha_2} s_{\alpha_3} \\ -c_{\alpha_1} s_{\alpha_2} c_{\alpha_3} + s_{\alpha_1} s_{\alpha_3} & -(c_{\alpha_1} s_{\alpha_3} + s_{\alpha_1} s_{\alpha_2} c_{\alpha_3}) & c_{\alpha_2} c_{\alpha_3} \end{pmatrix} \quad , \tag{2.13}$$

where the notation $sin(\alpha_i) \equiv s_{\alpha_1}$ and $cos(\alpha_i) \equiv c_{\alpha_1}$ was used. The mass matrix of these three scalars reads

$$M_N^2 = \begin{pmatrix} m_{22}^2 + \frac{1}{2}\bar{\lambda}_{345}v^2 & 0 & -\mathrm{Im}(A)v \\ 0 & m_{22}^2 + \frac{1}{2}\lambda_{345}v^2 & \mathrm{Re}(A)v \\ -\mathrm{Im}(A)v & \mathrm{Re}(A)v & m_S^2 + \frac{1}{2}\lambda_7 v^2 \end{pmatrix} \quad , \tag{2.14}$$

with $\bar{\lambda}_{345} = \lambda_3 + \lambda_4 - \lambda_5$ and $\lambda_{345} = \lambda_3 + \lambda_4 + \lambda_5$. It can be diagonalized via the rotation matrix to give the mass eigenvalues

$$RM_N R^T = \mathrm{diag}(m_{h_1}^2, m_{h_2}^2, m_{h_3}^2) \tag{2.15}$$

and are chosen such that

$$m_{h_1} \leq m_{h_2} \leq m_{h_3} \quad . \tag{2.16}$$

Since the particles $H^{\pm}$ and $h_{1,2,3}$ emerge from Φ_2 and Φ_S they have an odd $\mathbb{Z}_2$ symmetry and therefore carry a "dark charge" of -1 which is preserved in all interactions. In this thesis such particles will be referred to as Dark Sector (DS) particles. The lightest neutral state of these particles, h_1, will be the stable DM candidate in this model.

To see how this model provides additional CP violation consider the coupling Zh_ih_j which is obtained from

$$\left|D_\mu \Phi_2\right|^2 \supset \frac{g}{cos\theta_W}\left(R_{ij}R_{ji} - R_{ii}R_{jj}\right) Z_\mu \left(h_i\partial^\mu h_j - h_j\partial^\mu h_i\right) \quad . \tag{2.17}$$

Here, D_μ is the covariant derivative, g the $SU(2)_L$ coupling constant and θ_W the Weinberg angle.

This means that decays of the form $Z \longrightarrow h_ih_j$ and $h_i \longrightarrow Zh_j$ are simultaneously possible. One can try to figure out which CP quantum numbers the h_i's have by looking at these decays. Start with $Z \longrightarrow h_1h_2$ and, without loss of generality, assign a negative CP eigenvalue to h_1 and a positive one to h_2. Doing the same with h_1h_3 final states leads to a positive CP eigenvalue for h_3. However, now the process $Z \longrightarrow h_2h_3$ would be forbidden which is in contradiction with Eq. (2.17). This means the implicit assumption made here, that the h_i's have definite CP numbers was wrong. They are neither CP-even nor CP-odd but they are mixed CP states. The vertices in Eq. (2.17) can contribute at one-loop order to CP violating processes such as $Z \longrightarrow ZZ$ and $Z \longrightarrow W^+W^-$ [16].

2.3. Evidence for DM

As of today there are several observations and data that can be resolved by introducing DM. DM in this context does not necessarily need to be described by new BSM particles. Theories such as modified gravity [28] and primordial black holes [29] are other possible explanations of the phenomena that will be presented in this section.

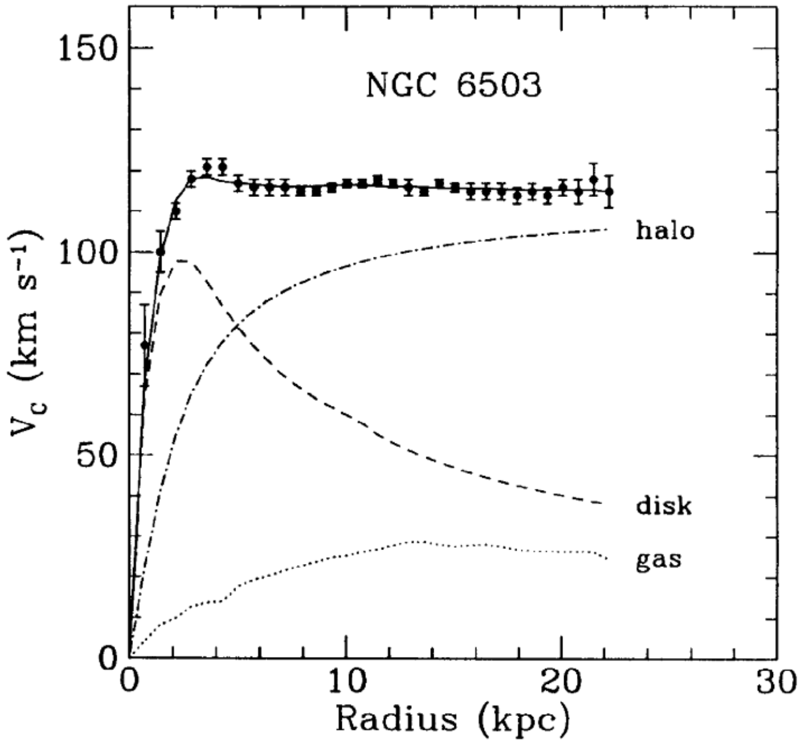

Figure 2.1.: Rotation curve velocity of galaxy NGC 6503 dependent on the distance from its center. The corresponding contributions from gas (dotted) and disk (dashed) are shown as well as the needed DM halo contribution (dash-dotted) to be compatible with the observed data [30].

2.3.1. Rotation Curves of Galaxies

One the biggest evidences towards the existence of DM, are the rotation curves of stars in different galaxies [12–14]. Observations of these galaxies revealed that the rotational velocities of stars in the outer parts of several galaxies are larger than expected. Models of the rotation curves of galaxies have to take into account the amount and distribution of gas and baryons as well as the shape of the bulge and the stellar disk. Under consideration of these factors the rotational curves with respect to the radius from the galactic center can be calculated. However, Fig. (2.1) shows that after taking all of these effects into account, the rotation curve velocities are well below the observed value, especially towards the outer parts of the disk. Only when assuming an additional DM halo around the galaxy, the observed data can be matched to the model.

2.3.2. Gravitational Lensing

Another important observation are the gravitational lensing effects of the bullet cluster [15]. This cluster has emerged from the collision of previously two separate clusters. During the collision of two clusters, galaxies can be viewed as collisionless particles while the X-ray emitting plasma between the galaxies can be viewed as a fluid that experiences

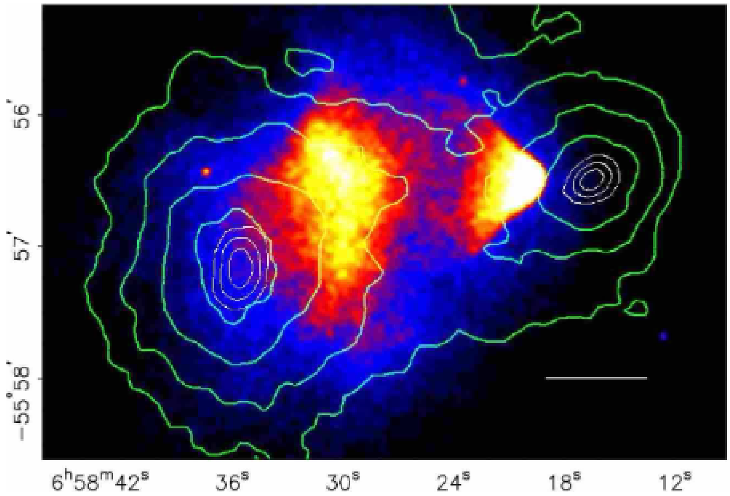

Figure 2.2.: Gravitational lensing effects in the bullet cluster. The heat map shows the density of the X-ray plasma fluid. The green lines show the lensing parameter κ with the value of the outer contour being $\kappa = 0.16$ and increasing in steps of 0.07 inwards [15].

pressure when passing through each other. This leads to a separation between the plasma, which has been slowed down by the exerted pressure, and the galaxies, which moved ahead of the plasma. In a setup with no DM, the main gravitational lensing effects would trace the visible X-ray plasma. With collisionless DM, however, the lensing shifts towards regions of high DM density. This region is expected to coincide with the position of the galaxies. Figure (2.2) shows the strength of gravitational lensing throughout the bullet cluster via the parameter κ. It shows that the largest values of κ and therefore gravitational lensing are located outside of the plasma bulk and at the positions of two separate galaxy concentrations. As already mentioned, this is can only occur if DM is involved.

2.3.3. Temperature Fluctuations in the CMB

The CMB consists of photons which decoupled from the thermal bath of the universe once they had no scattering partners. This was at $\sim 300000 - 400000$ years after the big bang, when free electrons began to be bound with protons to form hydrogen atoms, resulting in a sphere of last scattering. Since then, these photons have been moving freely in the universe. Due to the expansion of the universe their temperature kept decreasing reaching the measured value of today [31],

$$T_0 = (2.72548 \pm 0.00057)\,\mathrm{K} \quad . \tag{2.18}$$

This value shows variations of around $\delta T/T_0 \lesssim 10^{-5}$ on the sphere of last scattering. The study of these variations can give a clearer picture of how the early universe looked like and what it consisted of. A convenient way to describe the temperature fluctuations on the sphere of last scattering is via the spherical harmonics Y_{lm} in terms of the azimuthal and polar angles, ϕ and θ, respectively, [32]

$$\frac{\delta T(\theta,\phi)}{T_0} \equiv \frac{T(\theta,\phi)-T_0}{T_0} = \sum_{l=0}^{\infty}\sum_{m=-l}^{l} a_{lm}Y_{lm}(\theta,\phi) \quad . \tag{2.19}$$

The spherical harmonics form an orthonormal basis with respect to the integral over the solid angle $d\Omega = d\phi d\cos\theta$, i.e.

$$\int d\Omega Y_{lm}(\theta,\phi)Y^*_{kn}(\theta,\phi) = \delta_{lk}\delta_{mn} \quad . \tag{2.20}$$

To analyze temperature fluctuations, the relevant measure is the variance of the temperature distribution

$$\begin{aligned}\frac{1}{4\pi}\int d\Omega\left(\frac{\delta T(\theta,\phi)}{T_0}\right)^2 =& \frac{1}{4\pi}\int d\Omega\left[\sum_{l,m} a_{lm}Y_{lm}(\theta,\phi)\right]\left[\sum_{k,n} a^*_{kn}Y^*_{kn}(\theta,\phi)\right]\\ =& \frac{1}{4\pi}\sum_{l,m,k,n} a_{lm}a^*_{kn}\delta_{lk}\delta_{mn} = \frac{1}{4\pi}\sum_{lm}|a_{lm}|^2 \quad .\end{aligned} \tag{2.21}$$

The index m describes the angular momentum in one specific direction. However, since the sphere of last scattering does have any special direction, it implies that the coefficients a_{lm} do not depend on the value of m. This means that the sum over m gives $2l+1$ identical terms. With this the average of the $|a_{lm}|^2$ over m will be defined as the observed power spectrum

$$C_l \equiv \frac{1}{2l+1}\sum_{m=-l}|a_{lm}|^2 \quad . \tag{2.22}$$

Inserting into Eq. (2.21) results in

$$\frac{1}{4\pi}\int d\Omega\left(\frac{\delta T(\theta,\phi)}{T_0}\right)^2 = \sum_{l=0}^{\infty}\frac{2l+1}{4\pi}C_l \quad . \tag{2.23}$$

By measuring the temperature fluctuations, C_l can be obtained for different values of l. The measured power spectrum by PLANCK can be seen in Fig. (2.3). Since the average over m is taken, statistical fluctuations cancel out. However, for small l there are less independent orientations that can be measured, which lead to the large error bars shown. The peaks, which can be seen in the spectrum, are mainly generated through acoustic oscillations. These acoustic oscillations occur in the baryon-photon fluid at the time of photon decoupling. During this time, regions with a large accumulation of DM form gravitational wells, which pull the baryon-photon fluid inside it resulting in a compression of the fluid. At the same time the relativistic photons exert a pressure that counteracts the gravitational pull, which results in a rarefaction of the fluid. These counteracting forces create oscillations in the baryon-photon fluid and lead to temperature fluctuations in the photon spectrum during decoupling. The odd numbered peaks in the power spectrum correspond to the decoupling of photons during a compression phase, while even numbered peaks correspond to a decoupling during a rarefaction phase.

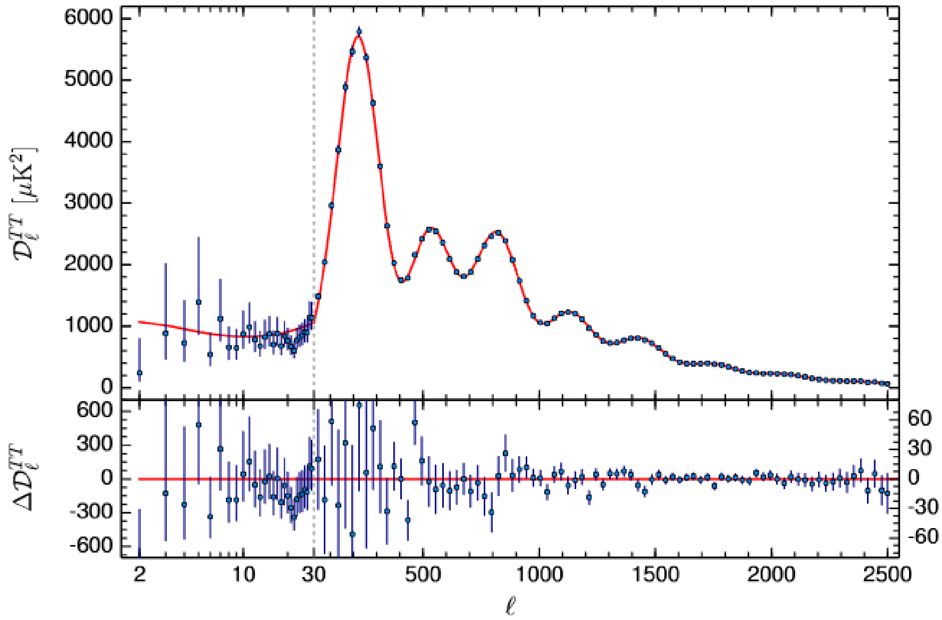

Figure 2.3.: Power spectrum of the CMB as measured by PLANCK [33].

The first peak corresponds to the time of last scattering where the fluid compressed once. Determining its position gives information about the curvature of the universe. The second peak corresponds to one compression and one rarefaction of the fluid. A large relative baryon content in the baryon-photon fluid would lead to an increase in amplitude of the compression peaks and at the same time to a decrease of the rarefaction peaks. Therefore, by measuring the ratio between the first and the second peak the baryon content of the universe can be obtained. The height of the third peak (2 compressions, 1 rarefaction) determines the amount of DM in the universe. Since, DM does not interact with photons, it only contributes to the strength of the compression peaks. Therefore, a large third peak is a sign of a sizeable DM component in the universe.

To fit the data points given in Fig. (2.3), a model with 6 independent cosmological parameters is used under the assumption of a flat universe. This model is referred to as the "base ΛCDM", where the parameters are the Hubble constant H_0, the baryon $\Omega_b h^2$ and DM $\Omega_c h^2$ densities, the matter fluctuation amplitude σ_8, the spectral index n_s and the optical depth τ [7]. Choosing the best fit parameters results in the observed relic density given in Eq. (1.2).

2.4. Detection of DM

Depending on the type of DM, different mass regions need to probed via direct or indirect detection experiments. In particle physics the possible DM candidates can be subdivided into two main categories - thermally and non-thermally produced DM. In this thesis the focus will lie on Weakly Interacting Massive Particles (WIMPs) and Feebly Interacting Massive Particles (FIMPs). Such types of DM are expected to be in the mass range of 1-1000 GeV and are produced thermally. On the other hand, non-thermally produced particles can range in mass from 10^{-22} eV to a few keV. Such particles are called Axion-Like Particles (ALPs) and were originally introduced to solve the strong CP problem [34].

In this section only detection experiments with respect to the WIMP paradigm will be presented. Experiments which are exclusively searching for ALPs like the Axion Dark Matter eXperiment (ADMX) [35], the Any Light Particle Search (ALPS) [36] and the CERN Axion Solar Telescope (CAST) [37] will not be discussed.

2.4.1. Indirect Detection

Indirect detection experiments search for SM particles which are produced via the annihilation of DM particles. This is done by looking at places in the universe with a large gravitational potential so that a large accumulation of DM is expected. One such experiment is done by the FERMI-LAT collaboration. Their analysis shows a photon excess coming from the center of the milky way galaxy [38]. This excess can be accounted for by DM annihilation into charged particles which then either decay or annihilate with other particles into photons. However, experiments of this sort do not give conclusive bounds for DM annihilation cross sections, since the same excess can be explained by a millisecond pulsar population [39].

2.4.2. Direct Detection

The goal of direct detection experiments is to detect collisions of DM particles with atomic nuclei. The differential cross section for the collision of a DM particle with a nucleon is given by [40]

$$\left(\frac{d\sigma}{dE_{\mathrm{R}}}\right)_{SI} = \frac{m_N}{2\mu_N^2 v^2}\left(\sigma_0^{\mathrm{SI}} F_{\mathrm{SI}}^2(E_{\mathrm{R}}) + \sigma_0^{\mathrm{SD}} F_{\mathrm{SD}}^2(E_{\mathrm{R}})\right) \quad , \tag{2.24}$$

with the recoil energy E_R of the nucleon in the non-relativistic limit

$$E_{\mathrm{R}} = \frac{\mu_N^2 v^2 (1-\cos\theta)}{m_N} \quad . \tag{2.25}$$

Further, $\mu_N = m_N m_\chi/(m_N + m_\chi)$ with the nucleon mass and DM mass m_N and m_χ, respectively, the relative velocity v between the nucleon and the DM particle and the scattering angle θ between the nucleon and the DM particle. The differential cross section consists of two terms on the r.h.s., the spin-independent term denoted by SI and the spin-dependent term denoted by SD with the corresponding cross sections σ_0 and nucleon form factors F^2. By calculating these cross sections via the coupling of the DM candidate to the constituents of the proton and neutron a prediction can be made on the expected direct detection cross section. Experiments, such as the `XENON1T` [41] and `LUX-ZEPLIN` (LZ) [42], search for such DM-nucleon collision events in large chambers filled with Xenon. By calculating the expected collision rate between DM and Xenon for the DM relic density

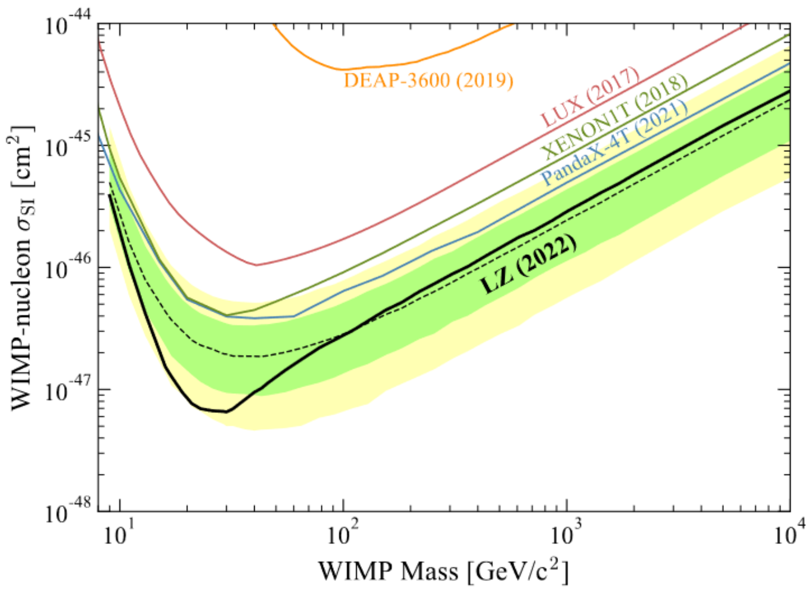

Figure 2.4.: Current exclusion limits of direct detection experiments. Regions above the lines are excluded by the corresponding experiments [42]. The green and yellow bands are the 1σ and 2σ sensitivity bands of the LZ limit.

given in Eq. (1.2), they can rule out certain regions in the plane of the DM-nucleon cross section and the DM mass if there are no collisions detected. Figure (2.4) shows the currently excluded regions of the SI cross section over the DM mass by several direct detection experiments. Currently, the strongest bound on the SI direct detection cross section is placed by the LZ experiment with a minimum value of $\sigma_{\mathrm{SI}} = 6.5 \cdot 10^{-48}$ cm^2 at a WIMP mass of 30 GeV.

There is, however, a problem future direct detection experiments will have to face. If the precision of these experiments keeps increasing they will begin to measure collisions between the nucleon and neutrinos coming from the sun, the atmosphere and supernovae. Such collisions would give a large background noise making it very difficult to differentiate between the background generated by neutrino collisions and possible DM collisions. This bound of when neutrino collisions start to become relevant is given by the neutrino floor [43] and is approximately 2 orders of magnitude below the current LZ bound.

2.4.3. Collider Searches

Collider searches try to detect DM by producing it at particle accelerators. The difficulty in finding DM particles at colliders is that DM particles do not decay and that they pass through the detectors due to their weak interaction with the SM. Because of this, production channels in which exactly two DM particles are produced cannot be distinguished from the event of two colliding particles just missing each other. Therefore, the only way to detect DM at colliders is through processes in which additional SM particles get produced and the missing momentum is analyzed. An example of such a process at an electron-positron

(e^+e^-) collider could be

$$e^+e^- \longrightarrow \chi\chi\gamma \quad , \tag{2.26}$$

where χ is the DM particle. Reconstructing the four-momentum of the photon γ, in this example, allows for a reconstruction of the four-momentum of the DM particles and therefore providing information about the mass and coupling to the SM of the DM candidate.

In addition to that, the ATLAS detector obtains a branching ratio for the Higgs boson into invisible particles with an expected limit of $\mathrm{BR}(h \longrightarrow \mathrm{inv.}) = 0.103$ [44]. This puts an upper limit on the coupling between the Higgs boson and possible DM candidates if they are below half the Higgs boson mass.

3. Mechanisms of Thermal DM Generation

This chapter gives a theoretical overview of two different types of thermal DM generation mechanisms. Sec. 3.1 deals with the phenomenology and relic density calculation via the freeze-out mechanism. The same will be done in Sec. 3.2 with the second mechanism, called freeze-in, and compared with the former. At last, in Sec. 3.3 the scenario of two DM candidates will be discussed.

3.1. Freeze-out

One of the possible mechanisms of generating WIMPs thermally is freeze-out. In this case the DM particles and SM particles start out in thermal equilibrium at the beginning of the universe. Furthermore the SM and DM particles interact with each other to stay in thermal equilibrium while also being able to annihilate. This means, that through the process below the same amount of DM is being created as annihilated

$$DM\,DM \longleftrightarrow SM\,SM \quad , \tag{3.1}$$

where DM and SM denote a DM and a SM particle, respectively. During the cooling of the universe all particles lose their kinetic energy. As a result, the heavy SM particles cannot be produced anymore. They start to decouple from the thermal bath and decay into lighter SM particles. At some point these lighter SM particles will not have enough energy to produce the heavy DM through the process (3.1). The DM however, will keep annihilating into the SM until a freeze-out temperature T_f is reached. This temperature is determined by the condition

$$\Gamma(T_f) \overset{!}{=} H(T_f) \quad . \tag{3.2}$$

Here Γ is the interaction rate of the annihilation process and H the Hubble expansion. This relation states that at a certain temperature the individual DM particles are too far apart from each other to interact and therefore to annihilate efficiently. Furthermore, to make the DM stable their decay into the SM has to be either forbidden or heavily suppressed.

3.1.1. One Particle Freeze-out

The evolution of the DM density from thermal equilibrium to present day, including freeze-out, for a single DM candidate χ is described by the Boltzmann Equation [32, 45]

$$\dot{n}(t) = -3H(t)n(t) - \langle\sigma v\rangle_{\chi\chi}(n(t)^2 - n_{\mathrm{eq}}^2) \quad , \tag{3.3}$$

with $n(t)$ being the particle density of the DM candidate at time t and n_{eq} its equilibrium density defined as

$$\begin{aligned} n_{\mathrm{eq}} &= g \int \frac{d^3p}{(2\pi)^3} f(E) \\ &= g \int \frac{d^3p}{(2\pi)^3} \frac{1}{e^{E/T} \pm 1} \quad . \end{aligned} \tag{3.4}$$

Here g are the internal degrees of freedom for a given particle and the integrand is the equilibrium distributions for fermions (+1) and bosons (-1) as function of the energy E of the particle. The Thermally Averaged Cross section (TAC) $\langle \sigma v \rangle_{\chi\chi}$ of two incoming DM particles with four momenta $p_{1/2}$ is defined as

$$\langle \sigma v \rangle_{\chi\chi} = \frac{\int d^3p_1 d^3p_2 f_1(E_1) f_2(E_2) \sigma_{\chi\chi} v_{12}}{\int d^3p_1 d^3p_2 f_1(E_1) f_2(E_2)} \equiv \frac{A}{D} \tag{3.5}$$

It is important to note that the cross section $\sigma_{\chi\chi}$ is a sum over all possible SM final states k and l, with

$$\sigma_{\chi\chi} = \sum_{k,l} \sigma_{\chi\chi,kl} \quad . \tag{3.6}$$

Denoted by v_{12} is the relative velocity between the incoming DM particles,

$$v_{12} = \frac{\sqrt{(p_1 p_2)^2 - m_1^2 m_2^2}}{E_1 E_2} \quad , \tag{3.7}$$

with the masses $m_1 = m_2 = m_\chi$ and $E_{1/2}$ the energies of the incoming DM particles.
At the freeze-out temperature the DM is assumed to be non-relativistic such that f can be approximated in the limit $T \ll m_\chi$ both for fermions and bosons by the Maxwell-Boltzmann distribution

$$f = e^{-E/T} \quad . \tag{3.8}$$

Inserting Eq. (3.8) into the numerator A of Eq. (3.5) and rewriting the integrals over the three momenta $\mathbf{p}_1$ and $\mathbf{p}_2$ by using the energy momentum relation ($i = 1, 2$)

$$\mathbf{p}_i^2 = E_i^2 - m_i^2 \quad , \tag{3.9}$$

one obtains

$$\begin{aligned} A = &\int d^3p_1 d^3p_2 \sigma_{\chi\chi} v_{12} e^{-(E_1+E_2)/T} \\ =&8\pi^2 \int dE_1 dE_2 dcos\theta E_1 E_2 |\mathbf{p_1}||\mathbf{p_2}| \sigma_{\chi\chi} v_{12} e^{-(E_1+E_2)/T} \quad , \end{aligned} \tag{3.10}$$

with θ being the angle between the two incoming DM particles. Following the prescription used in [45] a change of variables is performed as

$$\begin{aligned} E_+ \equiv &E_1 + E_2 \quad , \\ E_- \equiv &E_1 - E_2 \quad , \\ s \equiv &(p_1 + p_2)^2 = 2m_\chi^2 + 2E_1 E_2 - 2|\mathbf{p_1}||\mathbf{p_2}| cos\theta \quad , \end{aligned} \tag{3.11}$$

such that

$$dE_1 dE_2 dcos\theta \rightarrow \frac{dE_+ dE_- ds}{4|\mathbf{p_1}||\mathbf{p_2}|} \tag{3.12}$$

and the integration region $\{E_1, E_2 \geq m_\chi; -1 \leq cos\theta \leq 1\}$ transforms into

$$\begin{aligned} s \geq& (m_1 + m_2)^2 = 4m_\chi^2 \quad , \\ E_+ \geq& \sqrt{s} \quad , \\ 2p_{12}\sqrt{\frac{E_+^2 - s}{s}} \geq& \left| E_- - E_+ \frac{(m_1 - m_2)}{s} \right| \quad . \end{aligned} \tag{3.13}$$

Here,

$$p_{12} = \frac{\sqrt{(s - (m_1 + m_2)^2)(s - (m_1 - m_2)^2)}}{2\sqrt{s}} \quad , \tag{3.14}$$

denotes the center of mass momentum of the 2-DM particle system. Together with $E_1 E_2 v_{12} = p_{12}\sqrt{s}$ Eq. (3.10) becomes

$$A = 2\pi^2 \int dE_+ dE_- ds \, p_{12}\sqrt{s}\sigma_{\chi\chi} e^{-E_+/T} \quad . \tag{3.15}$$

Integrating over E_- and then E_+ gives

$$A = 8\pi^2 T \int ds \, p_{12}^2 \sqrt{s}\sigma_{\chi\chi} K_1 \left(\frac{\sqrt{s}}{T} \right) \quad . \tag{3.16}$$

Here K_1 is the modified Bessel function of the second kind.

Simplifying the denominator of Eq. (3.5) is more straight forward

$$\begin{aligned} D =& (4\pi)^2 \int dp_1 dp_2 p_1^2 p_2^2 e^{-(E_1+E_2)/T} \\ =& (4\pi)^2 \int dE_1 dE_2 E_1 E_2 \sqrt{E_1^2 - m_1^2}\sqrt{E_2^2 - m_2^2} e^{-(E_1+E_2)/T} \\ =& \left(4\pi \int_m^\infty dE E \sqrt{E^2 - m^2} e^{-E/T} \right)^2 \\ =& \left(4\pi m^2 T K_2 \left(\frac{m}{T} \right) \right)^2 \quad . \end{aligned} \tag{3.17}$$

Plugging Eqs. (3.16) and (3.17) back into Eq. (3.5) simplifies the TAC to

$$\langle \sigma v \rangle_{\chi\chi} = \frac{\int_{4m_\chi^2}^\infty ds \sqrt{s}(s - 4m_\chi^2) K_1(\sqrt{s}/T) \sigma_{\chi\chi}}{8m_\chi^4 T K_2^2(m_\chi/T)} \quad . \tag{3.18}$$

Going back to Eq. (3.3) it is clear from the right hand side that $\dot{n}(t)$ depends on two terms. The first term describes the drop off in particle density due to the expansion of the universe, while the other one is responsible for the drop off in density due to DM pair annihilation. Because the expansion term is independent of the model parameters it is not the crucial feature describing the final relic abundance. To get rid of it, a change of variables into the yield Y is performed

$$Y = \frac{n}{s'} \quad , \tag{3.19}$$

with the entropy density s'. Assuming constant entropy $S' = a^3 s'$ (here a is the scale factor) the relation below is obtained

$$\dot{Y} = \frac{\dot{n}}{s'} + 3s'\frac{\dot{a}}{a}\frac{n}{s'^2} = \frac{\dot{n}}{s'} + 3H\frac{n}{s'} \quad , \tag{3.20}$$

where $H = \frac{\dot{a}}{a}$ is the Hubble expansion and

$$\frac{dS}{dt} = 3a^2\dot{a}s' + a^3\dot{s}' = 0 \quad , \tag{3.21}$$

was used. Plugging Eq. (3.20) into Eq.(3.3) gives

$$\dot{Y} = -s'\langle\sigma v\rangle_{\chi\chi}(Y^2 - Y_{\text{eq}}^2) \quad . \tag{3.22}$$

Defining $x = m_\chi/T$ in order to switch to a temperature dependence the l.h.s. of Eq. (3.22) becomes

$$\frac{dY}{dx}\frac{dx}{dt} = \frac{dY}{dx}\left(-\frac{x}{T}\dot{T}\right) = \frac{dY}{dx}\left(-\frac{x}{T}\frac{ds'}{dt}\frac{dT}{ds'}\right) = \frac{dY}{dx}\left(3Hs'\frac{x}{T}\frac{dT}{ds'}\right) \quad . \tag{3.23}$$

Using the Friedmann equation in the early radiation dominated universe, which reads

$$H^2 = \frac{8\pi G\rho}{3} \quad , \tag{3.24}$$

together with the entropy density and energy density ρ dependent on the effective degrees of freedom h_{eff} with respect to the entropy and on the effective degrees of freedom g_{eff} with respect to energy as [46]

$$s' = h_{\text{eff}}(T)\frac{2\pi^2}{45}T^3 \quad , \quad \rho = g_{\text{eff}}(T)\frac{\pi^2}{30}T^4 \quad , \tag{3.25}$$

Eq. (3.23) can be rewritten as

$$\frac{dY}{dx} = -\sqrt{\frac{\pi}{45G}}\frac{g_*^{1/2}m_\chi}{x^2}\langle\sigma v\rangle_{\chi\chi}(Y^2 - Y_{\text{eq}}^2) \quad . \tag{3.26}$$

Here G is the gravitational constant and $g_*^{1/2}$ is defined as

$$g_*^{1/2} = \frac{h_{\text{eff}}}{\sqrt{g_{\text{eff}}}}\left(1 + \frac{T}{3h_{\text{eff}}}\frac{dh_{\text{eff}}}{dT}\right) \quad . \tag{3.27}$$

The equilibrium yield Y_{eq} in the non-relativistic limit is then given by

$$\begin{aligned} Y_{\text{eq}} =& \frac{n_{eq}}{s'} = \frac{1}{s'}\frac{g}{(2\pi)^3}\int d^3p\, e^{-E/T} = \frac{1}{s'}\frac{g}{2\pi^2}\int dEE\sqrt{E^2 - m_\chi^2}e^{-E/T} \\ =& \frac{1}{s'}\frac{g}{2\pi^2}m_\chi^2 TK_2\left(\frac{m_\chi}{T}\right) = \frac{45x^2}{4\pi^4 h_{\text{eff}}(m_\chi/x)}gK_2(x) \quad . \end{aligned} \tag{3.28}$$

By integrating Eq. (3.26) from the beginning of the universe $x = 0$ with the initial condition $Y(0) = Y_{\text{eq}}(0)$ to the current temperature T_0 of the CMB with $x_0 = m_\chi/T_0$ to obtain Y_0 of today, the relic density can be calculated via

$$\Omega_\chi = \frac{\rho_{\chi,0}}{\rho_{\text{c}}} = \frac{m_\chi n_0}{\rho_{\text{c}}} = \frac{m_\chi s_0 Y_0}{\rho_{\text{c}}} \quad . \tag{3.29}$$

Here, s_0 is the entropy density of today and $\rho_{\text{c}} = 3H^2/8\pi G$ the critical density which separates an expanding from a collapsing universe. To match the definition in Eq. (1.2) for the observed relic density, Eq. (3.29) is multiplied by the dimensionless constant

$$h^2 = \left(\frac{H}{100 \frac{\text{km}}{\text{s Mpc}}} \right)^2 \quad . \tag{3.30}$$

Inserting the corresponding numerical values gives

$$\Omega_\chi h^2 = m_\chi s_0 Y_0 \frac{8\pi G}{3H^2} h^2 \approx 2.742 \cdot 10^8 \frac{m_\chi}{\text{GeV}} Y_0 \quad . \tag{3.31}$$

3.1.2. Freeze-out in a Singlet Extension of the SM

To illustrate how Eq. (3.26) behaves for different TACs, consider the extension of the SM by a real singlet field Φ_S, which is the DM candidate. Requiring that the Lagrangian is invariant under the $\mathbb{Z}_2$ symmetry

$$\Phi \longrightarrow \Phi \ , \ \ \Phi_S \longrightarrow -\Phi_S \quad , \tag{3.32}$$

the most general renormalizable scalar potential reads

$$V = \mu^2 \Phi^\dagger \Phi + \lambda \left(\Phi^\dagger \Phi \right)^2 + \mu_S^2 \Phi_S^2 + \lambda_S \Phi_S^4 + \lambda_3 \Phi^\dagger \Phi \Phi_S^2 \quad . \tag{3.33}$$

Here, Φ is the SM scalar doublet with the corresponding parameters μ and λ which give the VEV in Eq. (2.3) and μ_S, λ_S as well as λ_3 are the free, real parameters of this model. Assuming that Φ_S has a VEV that is zero, the relevant interactions for freeze-out and the mass term for Φ_S after SSB are

$$V \supset \frac{1}{2}(2\mu_S^2 - \lambda_3 v)\Phi_S^2 + \lambda_3 v \, h \Phi_S^2 + \frac{\lambda_3}{2} h^2 \Phi_s^2 \quad , \tag{3.34}$$

where h is the Higgs field. The mass of the DM candidate is therefore given by

$$m_S = \sqrt{2\mu_S^2 - \lambda_3 v} \quad . \tag{3.35}$$

The interaction terms given by the second and third terms in Eq. (3.34) allow for annihilations of Φ_S into the SM particle pairs via the channels shown in Fig. (3.1). Such models are called Higgs portal models due to their connection to the SM via a Higgs mediator. This results in the annihilation cross section being proportional to λ_3^2, independent of the final

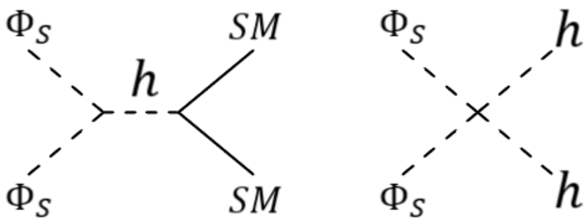

Figure 3.1.: Feynman diagrams of possible annihilation channels between Φ_S and the SM.

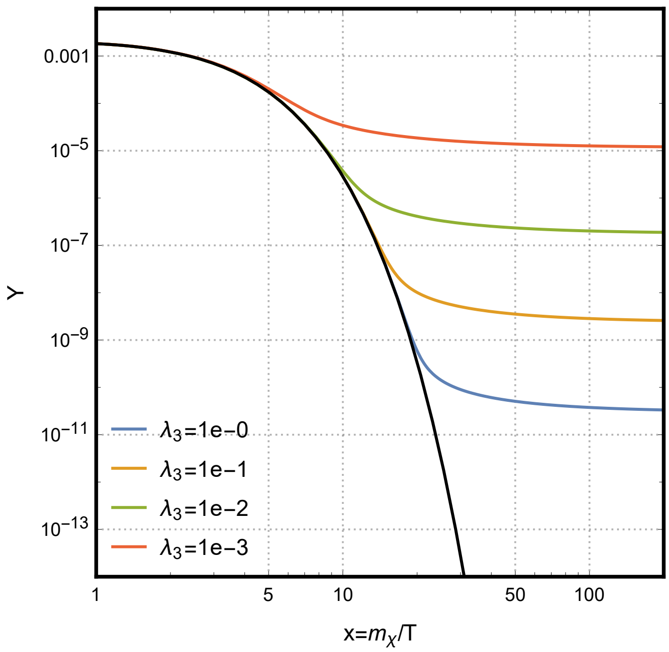

Figure 3.2.: Freeze-out via the $\Phi_S\Phi_S \longrightarrow b\bar{b}$ channel for $m_S = 100\,\text{GeV}$. The colored curves show the evolution of the yield for different portal couplings λ_3. The black curve shows the equilibrium yield Y_{eq}.

states.

It is clear from Eq. (3.18), that the TAC is proportional to the cross section (denoted by $\sigma_{\chi\chi}$ in Eq. (3.18)) and therefore also to λ_3^2. Figure (3.2) shows how $Y(x)$ evolves for different values of λ_3 and as result different TACs. Here, only the annihilation channel $\Phi_S\Phi_S \longrightarrow b\bar{b}$ is considered. It shows that for larger values of λ_3 the yield reaches a smaller constant value Y_0 and therefore via Eq. (3.31) a smaller relic density. This can be explained by the fact, that the TAC is a measure of how strongly the SM and DM bath are coupled to each other through the process (3.1). A large coupling allows for a better interaction rate. As a result of that, the condition (3.2) is fulfilled at a smaller temperature which translates into a larger x.

3.1.3. Multi Particle Freeze out

Equation (3.3) describes the simplest case in which the considered model has only one DS particle which is also the DM candidate. Many considered BSM models, however, have at least two or more DS particles in which the lightest of them is the DM candidate. In such cases an extension of Eq. (3.3) is necessary. Co-annihilation channels, scattering off the thermal background and decays have to be considered for each DS particle χ_i.
This section will closely follow the derivation by J. Edsjö and P. Gondolo [47] for the evolution of the density n_i of the DS particles χ_i. Extending Eq. (3.3) with the above mentioned processes gives

$$\begin{aligned}\dot{n}_i(t) + 3H(t)n_i(t) = &- \sum_j \langle\sigma v\rangle_{ij}(n_i n_j - n_{i,eq}n_{j,eq}) \\ &- \sum_{j\neq i}\left[\langle\sigma v\rangle_{X,ij}(n_i n_X - n_{i,eq}n_{X,eq}) - \langle\sigma v\rangle_{X,ji}(n_j n_X - n_{j,eq}n_{X,eq})\right] \\ &- \sum_{j\neq i}\left[\Gamma_{ij}(n_i - n_{i,eq}) - \Gamma_{ji}(n_j - n_{j,eq})\right] \quad . \end{aligned} \tag{3.36}$$

Equation (3.36) is a set of coupled differential equations describing the evolution of the density for each DS particle. The first term on the r.h.s. represents again the annihilation of two DS particles into the SM bath X

$$\chi_i\chi_j \to X \quad , \tag{3.37}$$

with the corresponding thermally averaged cross section denoted by $\langle\sigma v\rangle_{ij}$. Notice that this time the particle density of χ_i is not only influenced by the annihilation with another χ_i but also other DS particles χ_j with $i \neq j$. Such processes are called co-annihilation. The second term describes the scattering off the thermal background in the case that $i = j$ and conversions for $i \neq j$

$$\chi_i X \to \chi_j X \quad , \tag{3.38}$$

with the corresponding thermally averaged cross section denoted by $\langle\sigma v\rangle_{X,ij}$. Here, however, the state with $i = j$ is left out in the summation because it does not change the number of particles χ_i. Two terms have to be considered in this case. The first represents the conversion from a particle χ_i into all possible particles χ_j. While the second term represents the reverse process, namely the conversion of all χ_j particles into χ_i. Lastly, the third term takes the decays of the DS particles into consideration

$$\chi_i \to \chi_j X \quad , \tag{3.39}$$

with the corresponding decay width denoted by Γ_{ij}. Again, two terms are necessary to account for possible decays in both directions. The sum over $i = j$ is not needed for the same reason as for the previous term in addition to being kinematically forbidden.

Solving the differential equations (3.36) directly would take a large amount of computing power and therefore computing time. Here, however, an insight can be used to simplify

Eq. (3.36). Assuming that all the masses of the DS particles are different there has to be a lightest one, χ_1, with mass m_1 which represents the DM particle. This means that all the heavier particles eventually decay into χ_1 via the process (3.39). As a result the final DM density n is just the sum over all N DS particle densities

$$n = \sum_{i}^{N} n_i \quad . \tag{3.40}$$

By summing over i the second and third term in Eq. (3.36) cancel due to their symmetry in $i \leftrightarrow j$ resulting in

$$\dot{n}(t) + 3H(t)n(t) = -\sum_{i,j=1}^{N} \langle \sigma v \rangle_{ij} (n_i n_j - n_{i,eq} n_{j,eq}) \quad . \tag{3.41}$$

Considering that freeze-out occurs during the radiation dominated universe in which the SM particles are still relativistic while the DS particles are not, the density of the latter will be much lower because of the suppression factor coming from Eq. (3.8). This leads to a much larger scattering rate of $\sigma_{X,ij}$ relative to the annihilation rate of σ_{ij} causing the χ_i densities to stay in thermal equilibrium even when they start to decouple from the thermal bath before freeze-out. Specifically, the ratios between the individual particle densities and the total density are equal to their equilibrium values

$$\frac{n_i}{n} \simeq \frac{n_{i,eq}}{n_{\text{eq}}} \quad . \tag{3.42}$$

Equation (3.41) then becomes

$$\dot{n}(t) + 3H(t)n(t) = -\langle \sigma v \rangle_{\text{eff}} (n^2 - n_{\text{eq}}^2) \quad , \tag{3.43}$$

with

$$\langle \sigma v \rangle_{\text{eff}} = \sum_{i,j=1}^{N} \langle \sigma v \rangle_{ij} \frac{n_{i,eq} n_{j,eq}}{n_{\text{eq}}^2} \quad . \tag{3.44}$$

From here the same steps as in the previous section are applied to obtain the Boltzmann equation in terms of x and Y (cf. Eq. (3.26))

$$\boxed{\frac{dY}{dx} = -\sqrt{\frac{\pi}{45G}} \frac{g_*^{1/2} m_\chi}{x^2} \langle \sigma v \rangle_{\text{eff}} (Y^2 - Y_{\text{eq}}^2)} \quad . \tag{3.45}$$

The TAC is given by

$$\langle \sigma v \rangle_{\text{eff}} = \frac{\sum_{i,j=1}^{N} g_i g_j \int_{(m_i+m_j)^2}^{\infty} ds \sqrt{s} p_{ij}^2 \sigma_{ij}(s) K_1 \left(\frac{\sqrt{s} x}{m_1} \right)}{2T \left(\sum_{i=1}^{N} g_i m_i^2 K_2 \left(\frac{m_i}{m_1} x \right) \right)^2} \tag{3.46}$$

and the equilibrium density by

$$Y_{\text{eq}} = \sum_{i} Y_{\text{eq},i} = \frac{45 x^2}{4\pi^4 h_{\text{eff}}(x)} \sum_{i=1}^{N} g_i \left(\frac{m_i}{m_1} \right)^2 K_2 \left(\frac{m_i}{m} x \right) \quad . \tag{3.47}$$

The integrand of the numerator in Eq. (3.46) is the same as in Eq. (3.16) except for the additional sum over all possible initial states $\chi_i\chi_j$ with their respective internal degrees of freedom $g_{i/j}$. For the denominator the same is true but with Eq. (3.17) as the reference point.

Similar to the single DS particle case, the relic density decreases with a bigger TAC. However, in the multi DS particle scenario there are now more processes contributing to the TAC. A closer investigation of Eq. (3.46) reveals which initial states $\chi_i\chi_j$ give the highest contribution to the final relic abundance. The first step is to approximate the Bessel functions for $\tilde{x} \longrightarrow \infty$ by [48]

$$K_n(\tilde{x}) \sim \sqrt{\frac{\pi}{2x}} e^{-\tilde{x}} \left[1 + \frac{4n^2 - 1}{8\tilde{x}} + \frac{(4n^2-1)(4n^2-9)}{2!(8\tilde{x})^2} + ... \right] \quad . \tag{3.48}$$

Already for $\tilde{x} = 10$ the difference between the approximation and the exact function becomes negligible. Typical freeze-out temperatures are at $x = m_1/T \approx 25$, justifying this approximation. The important part of Eq. (3.48) is the exponential dependence which represents the Boltzmann suppression factor. This means that when integrating over s in the numerator of Eq. (3.46) the highest contribution of all initial states is at their rest mass. Another consequence is that contributions of initial states whose rest mass is significantly higher than $2m_1$ are suppressed by the exponential factor. A rough estimate gives

$$\frac{K_1\left(\frac{(m_i+m_j)x}{m_1}\right)}{K_1\left(\frac{2m_1 x}{m_1}\right)} \propto e^{-\frac{x}{m_1}(m_i+m_j-2m_1)} \quad . \tag{3.49}$$

To get a sense of how strong this suppression is consider the initial state $\chi_1\chi_2$ with $m_2 = 1.5 \cdot m_1$ and $x = 25$. Equation (3.49) returns a value of approximately $4 \cdot 10^{-6}$. This means that by the time the freeze-out of DM occurs co-annihilations with χ_2 will be almost irrelevant. In other words: to obtain efficient co-annihilation channels the masses of the DS particles have to be close to the lightest one.

Another way to make sense of this conclusion is by thinking of the phenomenology behind it. Again, consider only two DS particles χ_1 and χ_2 whose masses are far apart and where χ_1 is the DM candidate. At the beginning of the universe everything is in equilibrium via the process (3.37) and its reverse. When the universe starts to cool down the heavier particles χ_2 start to decouple from the thermal bath. They now have a much higher density than they would have had if they remained in thermal equilibrium. It would be reasonable to expect that co-annihilations with χ_1 get enhanced and therefore reduce the relic density. However, the processes (3.38) and (3.39) convert all the χ_2 particles into χ_1's at a rate many orders of magnitude larger than co-annihilations can take place, pulling them back into thermal equilibrium. One might expect that the density of χ_1 shoots up because of these processes. This is not the case though, because χ_1 is still in thermal equilibrium with the SM. As soon as the density of χ_1 gets larger than its equilibrium value, the process

$$\chi_1\chi_1 \longrightarrow X \tag{3.50}$$

gets enhanced and brings it back into equilibrium. Therefore, when the masses are far apart, neither the decays and conversions of χ_2 into χ_1 are relevant for the final relic density, nor the co-annihilations.

In the case that the masses of the two particles are close to each other the same steps can be followed. The difference this time is that now shortly after χ_2 decouples χ_1 starts to decouple from the thermal bath as well. Which means that the processes (3.50) is already heavily suppressed and χ_1 has not enough time to give the additional density it gains from χ_2 due to decays and conversions back to the thermal bath and keeps it instead. This leads to an increase of the relic density. At the same time, conversions are not as favored in one direction as they were in the previous case. As a consequence the density of χ_2 does not go back into thermal equilibrium as quickly and allows for co-annihilations to take place for a significant period of time. This leads to the reduction of the relic density in contrast to the increase from decays and conversions. Depending on how large the co-annihilation cross section is this will finally lead to either an increase or decrease of the relic density. The condition for a decrease in relic density due to co-annihilation reads

$$\langle \sigma v \rangle_{\text{eff}} > \langle \sigma v \rangle_{11} \quad . \tag{3.51}$$

Upon further investigation of Eq. (3.46) one might notice that the largest contribution in the numerator of the TAC is not only determined by the Boltzmann suppression factor ($K_1\left(\sqrt{s}x/m_1\right)$) but also by the annihilation cross section σ_{ij}. This can lead to a scenario where the annihilation of χ_2 pairs into the SM will be the main contributor to the final relic density. Phenomenologically speaking this means that χ_2 can freeze out at a much later time than χ_1 despite being the heavier of the two, i.e. if $\sigma_{22} \gg \sigma_{11}$ and $m_{\chi_1} \approx m_{\chi_2}$. Since χ_1 freezes out earlier and is not able to decay into χ_2 it would be reasonable to expect that its density is the main contributor to the final relic density. However, this is not the case as already stated above. When the χ_1 particles decouple from the bath their density will be much larger than the density of χ_2 which leads to an enhancement of the conversion process

$$\chi_1 X \to \chi_2 X \quad . \tag{3.52}$$

This process pulls the χ_1 density back to its equilibrium value until χ_2 itself starts to freeze-out. Due to the decays of χ_2 particles into χ_1 particles, the density of the former determines the final DM relic density.

3.2. Freeze-in

The problem with freeze-out is that when the coupling to the SM gets very small the DM annihilations are not efficient enough to produce the current relic density. In this regime of very weakly interacting massive particles, also called Feebly Interacting Massive Particles (FIMPs) another mechanism can take place - the so called freeze-in. In contrast to freeze-out the DM particles do not start in thermal equilibrium with the SM but with no initial abundance. Which means that process (3.1) favors the direction of DM production from SM particles instead of annihilation of DM particles into SM particles. This production

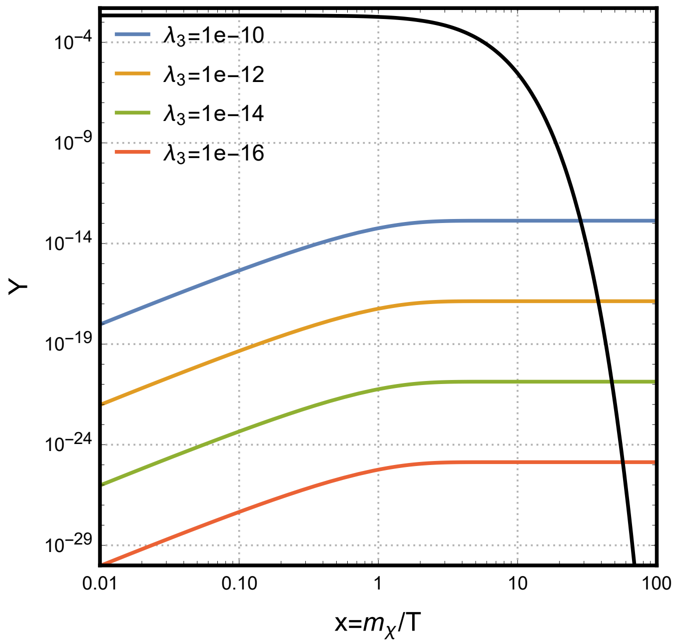

Figure 3.3.: Freeze-in via the $\Phi_S \Phi_S \longrightarrow b\bar{b}$ channel for $m_S = 100\,\text{GeV}$. The colored curves show the evolution of the yield for different portal couplings λ_3. The black curve shows the equilibrium yield Y_{eq}.

happens until the condition in Eq. (3.2) applies and the SM coupling to the DM is too small to accommodate for the expansion of the universe.

The calculation of the relic density via freeze-in is in general more involved than for freeze-out. Due to the fact that during freeze-in the DM particles are not in thermal equilibrium with the SM particles, the newly produced heavy DM particles have in general less kinetic energy than at equilibrium and Eq. (3.8) does not necessarily apply [49, 50]. One has to make sure that newly produced DM particles are in kinetic equilibrium with the thermal bath. Processes like (3.38) with $i = j$ need to have interaction rates large enough to keep the DM candidate in kinetic equilibrium. Because freeze-in begins at the reheating temperature of the universe and ends at $x \approx 2 - 5$ [51], the DM particles are relativistic throughout most of the process so that the approximation in Eq. (3.42) can not be applied. This means that Eq. (3.41) has to be used to calculate the freeze-in for multiple DS particles. In terms of Y and x the Boltzmann equation becomes

$$\frac{dY}{dx} = \sqrt{\frac{\pi}{45G}} \frac{g_*^{1/2} m_\chi}{x^2} \sum_{i,j=1}^{N} \langle \sigma v \rangle_{ij} (Y_{i,eq} Y_{j,eq} - Y_i Y_j) \quad . \tag{3.53}$$

It is important to note that the equation only works if the DS particles are in kinetic equilibrium with the SM. Figure (3.3) shows the relation between the coupling λ_3 from the potential (3.33) and the evolution of Y. As for to freeze-out a higher value of λ_3 results in a larger TAC. In contrast to freeze-out though, a larger TAC results in a larger yield (and therefore relic density), because the annihilation of SM particles into DM is more efficient.

Another possible process that can contribute to the final relic density in the freeze-in scenario are decays of SM particles into the DS. In such cases Eq. (3.53) has to be extended by a decay rate $\Gamma_{X\to ij}$. In this thesis such processes will not be considered due to the large masses of the DS particles that will be considered in *CP in the Dark*.

3.3. Two DM Candidates

The previous sections focused on models in which all the particles in the DS eventually decay into the DM candidate. However it is possible to introduce additional DM candidates by imposing more symmetries. One way to accomplish this is by introducing two symmetries $\mathbb{Z}_2$ and $\mathbb{Z}_2'$ and extending the scalar sector of the SM by two real singlets χ and ψ with the following transformation properties under $\mathbb{Z}_2$,

$$X \to X \ , \ \ \chi \to -\chi \ , \ \ \psi \to \psi \ \ , \tag{3.54}$$

and under $\mathbb{Z}_2'$

$$X \to X \ , \ \ \chi \to \chi \ , \ \ \psi \to -\psi \ \ , \tag{3.55}$$

where X denotes the SM particles. In such a case both of the singlets are stable DM candidates. To compute the relic density two coupled Boltzmann equations for both particles have to be solved

$$\frac{dY_\chi}{dx} = -\sqrt{\frac{\pi}{45G}}\frac{g_*^{1/2} m_\chi}{x^2}\left[\langle\sigma v\rangle_{\chi\chi X}(Y_\chi^2 - Y_{\chi,eq}^2) + \langle\sigma v\rangle_{\chi\chi\psi\psi}\left(Y_\chi^2 - \frac{Y_\psi^2}{Y_{\psi,eq}^2}Y_{\chi,eq}^2\right)\right] \quad , \tag{3.56}$$

$$\frac{dY_\psi}{dx} = -\sqrt{\frac{\pi}{45G}}\frac{g_*^{1/2} m_\chi}{x^2}\left[\langle\sigma v\rangle_{\psi\psi X}(Y_\psi^2 - Y_{\psi,eq}^2) - \langle\sigma v\rangle_{\chi\chi\psi\psi}\left(Y_\chi^2 - \frac{Y_\psi^2}{Y_{\psi,eq}^2}Y_{\chi,eq}^2\right)\right] \quad , \tag{3.57}$$

where $\langle\sigma v\rangle_{\chi\chi X}$ and $\langle\sigma v\rangle_{\psi\psi X}$ is the TAC for the annihilation of two χ and ψ particles into the SM bath, respectively. The TAC $\langle\sigma v\rangle_{\chi\chi\psi\psi}$ represents the annihilation process $\chi\chi \to \psi\psi$. In this case the relic density is given by

$$\Omega h^2 = (\Omega_\chi + \Omega_\psi)h^2 = 2.742 \cdot 10^8 \left(\frac{m_\chi}{\text{GeV}}Y_{0,\chi} + \frac{m_\psi}{\text{GeV}}Y_{0,\psi}\right) \quad . \tag{3.58}$$

With $Y_{0,\chi}$ and $Y_{0,\psi}$ being the yields at the current CMB temperature for χ and ψ, respectively.

The first term on the r.h.s. of each equation corresponds to the already discussed connection to the SM bath. On the other hand the second term in both equations introduces an interaction between χ and ψ via pair annihilation and creation. The term is identical in both equations apart from the opposite signs which correspond to annihilation and creation of the particles. Another important aspect is the additional enhancement factor

$$\bar{Y}_\psi^2 = \frac{Y_\psi^2}{Y_{\psi,\text{eq}}^2} \quad . \tag{3.59}$$

Consider the scenario in which both χ and ψ go through the freeze-out process and $m_\psi > m_\chi$. They both start in thermal equilibrium, therefore $\bar{Y}_\psi = 1$. At some point ψ starts to freeze-out and it moves from thermal equilibrium to a constant Y_ψ value before χ begins to freeze-out. The equilibrium yield of ψ, however, will keep dropping hence increasing $\bar{Y}_\psi$. This enhancement factor is a measure of how much bigger the density of the particle is compared to its equilibrium value. Because the SM is always in thermal equilibrium during freeze-out the corresponding terms do not have such enhancement factors.

4. Freeze-in in CP in the Dark

This chapter starts of by determining the conditions for freeze-in for the model *CP in the Dark* in Sec. (4.1). In Sec. (4.2) the implications of the freeze-in scenario will be investigated. The corresponding Boltzmann equations for such a scenario will be derived in Sec. (4.3).

4.1. Freeze-in Conditions

In Ref. [16] it is shown that freeze-out is possible in *CP in the Dark* for numerous allowed parameter points. Therefore, this chapter will take closer a look at the possibility of freeze-in in *CP in the Dark*.

In the previous chapter the two DM generation mechanisms were discussed independently of each other. However, in *CP in the Dark*, it is possible to have both of these mechanisms contributing to the same final relic density. Under the right conditions it can happen that some DS particles freeze out while others freeze in. In this chapter such processes will be analyzed and their viable parameter regions will be discussed.

The first step is to look at the coupling strengths between the DS particles and the SM particles. For the particles that freeze out, the coupling strength has to be at least of order 10^{-3}, while for the particles which freeze in it has to be a maximum of 10^{-10} [51]. In order to achieve such a low coupling, the rotation matrix in Eq. (2.13) has to be chosen in such way that one of the h_i decouples from the Z and W bosons otherwise the $SU(2)$ gauge coupling is too large for freeze-in to occur since it is proportional to $g/\cos\theta_W \approx 0.74 \gg 10^{-10}$.

First, consider the decoupling of h_1. Here, the absolute value of the couplings for the vertices Zh_1h_2 and Zh_1h_3 have to be minimized. Inserting the definition of the rotation matrix into Eq. (2.17) and simplifying gives

$$\left|D_\mu \Phi_2\right|^2 \ni \frac{-g}{cos\theta_W} c_{a_2} c_{a_3} Z_\mu \left(h_1 \partial^\mu h_2 - h_2 \partial^\mu h_1\right) \quad \text{for} \;\; i = 1, \;\; j = 2 \;\; \text{and} \tag{4.1}$$

$$\left|D_\mu \Phi_2\right|^2 \ni \frac{g}{cos\theta_W} c_{a_2} s_{a_3} Z_\mu \left(h_1 \partial^\mu h_3 - h_3 \partial^\mu h_1\right) \quad \text{for} \;\; i = 1, \;\; j = 3 \quad . \tag{4.2}$$

This means that the couplings go to zero for $\alpha_2 \longrightarrow \frac{\pi}{2}$ and the rotation matrix becomes

$$R = \begin{pmatrix} 0 & 0 & 1 \\ -s_{\alpha_1+\alpha_3} & c_{\alpha_1+\alpha_3} & 0 \\ -c_{\alpha_1+\alpha_3} & -s_{\alpha_1+\alpha_3} & 0 \end{pmatrix} \quad . \tag{4.3}$$

Now inserting into Eq. (2.12) it becomes clear why the states decouple in this regime

$$\begin{aligned} h_1 &= \Phi_s \quad , \\ h_2 &= -\, s_{\alpha_1+\alpha_3}\rho + c_{\alpha_1+\alpha_3}\eta \quad , \\ h_3 &= -\, c_{\alpha_1+\alpha_3}\rho - s_{\alpha_1+\alpha_3}\eta \quad . \end{aligned} \tag{4.4}$$

The fields of the $SU(2)$ doublet ρ and η do not contribute to the h_1 mass eigenstate. This means that it no longer has any interaction with W or Z bosons. The whole weak coupling strength that h_1 could have had, has been rotated into h_2 and h_3. Another consequence of such a rotation is that the model loses its additional CP violation. Since decays of the type $Z \to h_1 h_{2/3}$ are now forbidden, the mass eigenstates can be assigned definite CP quantum numbers. More consequences of such a rotation will be discussed in the next section.

The gauge coupling is not the only one that has to be kept small. The other couplings to the SM (Φ_1) have to be checked as well. By looking at Eq. (2.6), only λ_{3-5}, λ_7 and A come into question. Here, λ_{3-5} can be disregarded since they only describe the couplings between the dark $SU(2)$ doublet and the SM. This means that only λ_7 and A have to be kept small for freeze-in, since they are the couplings between the singlet field and the SM doublet.

Decoupling h_1 via Eq. (4.3) is of course an arbitrary choice and one could instead decouple h_2 or h_3. By setting $\alpha_2 = 0$ and $\alpha_3 = \frac{\pi}{2}$ the rotation matrix gives

$$R = \begin{pmatrix} c_{\alpha_1} & s_{\alpha_1} & 0 \\ 0 & 0 & 1 \\ s_{\alpha_1} & -c_{\alpha_1} & 0 \end{pmatrix} \quad . \tag{4.5}$$

In this case h_2 becomes the singlet particle while h_1 and h_3 stem from the mixing of the doublet fields. The same can be done with $\alpha_2 = 0$ and $\alpha_3 = 0$ to make the h_3 the singlet particle. However, the analysis will be the same as with h_1 as the singlet particle and the couplings are therefore constrained in the same way. The rotation matrix just determines which mass eigenstates are part of the $SU(2)$ doublet and which one is the singlet. This also shows that a scenario in which all the DS particles freeze-in is not possible because the $SU(2)$ coupling strength can only be rotated to different particles but not reduced overall.

In this thesis the focus will be on h_1 being the singlet because in this case only one of the angle parameters has to be fixed leaving more parameter space open to be scanned.

4.2. Implications of the Decoupling Limit

The Higgs sector of *CP in the Dark* needs 13 parameters to be fully described. In this thesis, they are chosen to be

$$v,\ m_h^2,\ m_{22}^2,\ m_S^2,\ m_{h_1},\ m_{h_2},\ m_{H^\pm},\ \alpha_1,\ \alpha_2,\ \alpha_3,\ \lambda_2,\ \lambda_6,\ \lambda_8 \quad . \tag{4.6}$$

From these the rest of the parameters can be calculated via the relations given in Appendix A.1. As already mentioned in the previous section, λ_7 and A have to be kept small in order for h_1 to able to freeze-in. Inserting $\alpha_2 = \frac{\pi}{2}$ into Eqs. (A.5-A.7) results in

$$\lambda_7 = \frac{2(m_{h_1}^2 - m_S^2)}{v^2} \quad \text{and} \quad A = 0 \quad . \tag{4.7}$$

Therefore, the condition for a small λ_7 is that $m_{h_1}^2 \approx m_S^2$, which corresponds to a small coupling to the Higgs boson. The second result from Eq. (4.7) has a larger consequence. The parameter A determines the coupling strength for decays of the form $h_{2/3} \longrightarrow hh_1$. Setting it to zero forbids such decays. Now all decay channels of the DS particles which freeze-out into h_1 are blocked. This means, that the lightest particle among the ones that freeze-out is also a DM candidate. By setting $A = 0$ the theory obtains a higher symmetry. Looking at the potential of the model in Eq. (2.6) it becomes clear that setting this parameter to zero is the same as imposing a second $\mathbb{Z}_2$ symmetry. The limit $\alpha_2 = \frac{\pi}{2}$ imposes the following transformation behaviour under $\mathbb{Z}_2$

$$X \longrightarrow X \ , \ \ \Phi_S \longrightarrow -\Phi_S \ , \ \ \Phi_2 \longrightarrow \Phi_2 \quad , \tag{4.8}$$

and $\mathbb{Z}_2'$

$$X \longrightarrow X \ , \ \ \Phi_S \longrightarrow \Phi_S \ , \ \ \Phi_2 \longrightarrow -\Phi_2 \quad , \tag{4.9}$$

where X is some SM particle. Even more, by looking at Eqs. (A.1) and (A.4) it follows that $m_{h_3} = m_{h_2}$, which results in the degeneracy of the particles h_2 and h_3 with the consequence of making them the two DM candidates in the freeze-out sector. From this degeneracy, together with $\alpha = \pi/2$, it follows that $\lambda_5 = 0$. Due to this, all coupling strengths between $h_{2/3}$ and the SM are identical (see Appendix A.2), meaning that they obtain the same yield via freeze-out.

To reiterate, the goal was to find a region in the parameter space in which freeze-in is possible. It turns out that for one particle (in this case h_1) it is possible if $\alpha_2 = \frac{\pi}{2}$, otherwise the $SU(2)$ gauge couplings become too strong. However, fixing this angle leads to a higher symmetry with two additional DM candidates. This results in a scenario in which h_1 goes through the freeze-in process, while $h_{2/3}$ and $H^{\pm}$ freeze-out. The equations to calculate the relic density of such a system will be discussed in the next section.

4.3. Boltzmann Equations

As already discussed in Sec. (3.3) the scenario with two DM candidates involves solving two coupled differential equations, which read [52, 53]

$$\frac{dY_1}{dx} = \sqrt{\frac{\pi}{45G}} \frac{g_*^{1/2} m_\chi}{x^2} \left[\langle\sigma v\rangle_{11X} (Y_{1,\text{eq}}^2 - Y_1^2) + \sum_i \langle\sigma v\rangle_{11ii} \left(\frac{Y_i^2}{Y_{i,\text{eq}}^2} Y_{1,\text{eq}}^2 - Y_1^2 \right) \right] \quad , \tag{4.10}$$

$$\frac{dY_\text{f}}{dx} = -\sqrt{\frac{\pi}{45G}} \frac{g_*^{1/2} m_\chi}{x^2} \left[\langle\sigma v\rangle_\text{eff} (Y_\text{f}^2 - Y_{\text{f,eq}}^2) - \sum_i \langle\sigma v\rangle_{11ii} \left(Y_1^2 - \frac{Y_i^2}{Y_{i,\text{eq}}^2} Y_{1,\text{eq}}^2 \right) \right] \quad . \tag{4.11}$$

The first equation determines the density of h_1 via freeze-in. Here, $\langle\sigma v\rangle_{11X}$ is the TAC for $2 \to 2$ processes between h_1 and the SM, where the sum over all possible SM final states is implicit. Furthermore, $\langle\sigma v\rangle_{11ii}$ is the TAC for annihilation of two h_1s into two DS particles of the thermal bath. The second equation describes the freeze-out of the other DS particles where f denotes the whole DS bath and i the individual particles. In this case Eq. (3.45) was used for the first term, where $\langle\sigma v\rangle_{\text{eff}}$ is given by Eq. (3.46).

Eqs. (4.10) and (4.11) can be simplified by assuming that the density of h_1 is much lower than its equilibrium value. This approximation holds for freeze-in since h_1 starts with no initial abundance and remains below the equilibrium density throughout the whole process. As a result of that, terms proportional to Y_1^2 can be neglected. On top of that the approximation used in Eq. (3.42) can be reused for the enhancement factors in both equations such that

$$\frac{Y_i^2}{Y_{i,\text{eq}}^2} = \frac{Y_\text{f}^2}{Y_{\text{f,eq}}} \equiv \overline{Y}_\text{f}^2 \quad . \tag{4.12}$$

Applying these approximations gives

$$\frac{dY_1}{dx} = \sqrt{\frac{\pi}{45G}}\frac{g_*^{1/2} m_\chi}{x^2}\left[\langle\sigma v\rangle_{11X} Y_{1,\text{eq}}^2 + \langle\sigma v\rangle_{11\text{f}} \frac{Y_\text{f}^2}{Y_{\text{f,eq}}^2} Y_{1,\text{eq}}^2\right] \quad , \tag{4.13}$$

$$\frac{dY_\text{f}}{dx} = -\sqrt{\frac{\pi}{45G}}\frac{g_*^{1/2} m_\chi}{x^2}\left[\langle\sigma v\rangle_{\text{eff}}(Y_\text{f}^2 - Y_{\text{f,eq}}^2) + \langle\sigma v\rangle_{11\text{f}} \frac{Y_\text{f}^2}{Y_{\text{f,eq}}^2} Y_{1,\text{eq}}^2\right] \quad , \tag{4.14}$$

where

$$\sum_i \langle\sigma v\rangle_{11ii} = \langle\sigma v\rangle_{11\text{f}} \quad . \tag{4.15}$$

To obtain the relic density, the coupled differential equations (4.13) and (4.14) have to be solved. However, by looking at Figs. (3.2) and (3.3) it becomes clear that freeze-out and freeze-in occur at different times during the evolution of the universe. Typical freeze-out temperatures T_FO, which do not result in an over abundance of the relic density, are at $x_\text{FO} = m/T_\text{FO} \approx 23 - 28$ [54]. While freeze-in typically ends at temperatures T_FI of $x_\text{FI} = m/T_\text{Fi} \approx 2 - 5$ [51]. In the case considered here, the freeze-out and freeze-in temperatures with respect to the DM masses are at

$$x_\text{FO} = \frac{m_{h_{2/3}}}{T_\text{FO}} \quad , \tag{4.16}$$

$$x_\text{FI} = \frac{m_{h_1}}{T_\text{FI}} \quad . \tag{4.17}$$

Suppose that $m_{h_{2/3}} \approx m_{h_1}$, this implies that throughout the whole freeze-in process of h_1, $h_{2/3}$ are in thermal equilibrium and therefore $\overline{Y}_\text{f}^2 = 1$.

If, however, the masses of h_1 and $h_{2/3}$ are far apart such that the temperatures of freeze-out and freeze-in overlap, the enhancement factor becomes non-unity during freeze-in. The needed mass ratio between the DM candidates can be obtained via the condition $T_{\mathrm{FO}} \stackrel{!}{=} T_{\mathrm{FI}}$ and Eqs. (4.16) and (4.17) to

$$\frac{m_{h_{2/3}}}{m_{h_1}} \approx 4.6 - 14 \quad , \tag{4.18}$$

for the typical freeze-out and freeze-in temperatures mentioned above. On the other hand, such high mass ratios lead to a small TAC as can be seen in the numerator of Eq. (3.18). This counteracts the enhancement, such that it does not contribute in this regime. As a consequence the enhancement factors can be neglected, independent of when freeze-out occurs.

Another point, is that due to the difference in coupling strengths between freeze-out and freeze-in, it follows that $\langle\sigma v\rangle_{11\mathrm{f}} \ll \langle\sigma v\rangle_{\mathrm{eff}}$. Therefore, $\langle\sigma v\rangle_{11\mathrm{f}}$ can be neglected in Eq. (4.14). This means that Eqs. (4.13) and (4.14) decouple to

$$\frac{dY_1}{dx} = \sqrt{\frac{\pi}{45G}}\frac{g_*^{1/2} m_\chi}{x^2}\left[\langle\sigma v\rangle_{11X} + \langle\sigma v\rangle_{11\mathrm{f}}\right] Y_{1,\mathrm{eq}}^2 \quad , \tag{4.19}$$

$$\frac{dY_{\mathrm{f}}}{dx} = -\sqrt{\frac{\pi}{45G}}\frac{g_*^{1/2} m_\chi}{x^2}\langle\sigma v\rangle_{\mathrm{eff}}(Y_{\mathrm{f}}^2 - Y_{\mathrm{f,eq}}^2) \quad , \tag{4.20}$$

Notice, that conversion processes of the type

$$h_i X \to h_1 X \quad \text{and} \tag{4.21}$$

$$h_i h_j \to h_k h_1 \quad , \tag{4.22}$$

do not need to be included because all of them have a vertex of the type $X h_1 h_{2/3}$, which is zero when $\alpha_2 = \pi/2$ (see Appendix A.2).

5. Applied Constraints

To reiterate, the goal is to find a viable scenario in which the DM particle h_1 obtains its relic density via freeze-in, while the other DM particles h_2 and h_3, including the co-annihilations with $H^{\pm}$, obtain their relic density via freeze-out. In order to get viable parameter scenarios, scans are performed in the parameter space of the model and only those parameter points are kept that fulfill the most relevant theoretical and experimental constraints, besides the constraints from the relic density. The code `ScannerS` [20, 21] allows to perform parameter scans in the parameter space of the model and to check each parameter point for the following requirements:

- The correct value of the observed mass of the Higgs boson has to be obtained and the correct electroweak symmetry breaking needs to occur. This is ensured by requiring that $v = 246.22$ GeV in Eq. (2.10) and that the parameters fulfill Eq. (2.9) and the first relation given in Eq. (2.11).

- Tree-level pertubative unitarity needs to be fulfilled for all $2 \to 2$ scalar scattering processes. `ScannerS` therefore demands that for every eigenvalue of the scalar tree-level $2 \to 2$ scattering matrix $M^i_{2\to 2}$ the following condition is fulfilled [55]
$$\left|M^i_{2\to 2}\right| \leq 8\pi \quad . \tag{5.1}$$

- The strength of the quartic couplings of the *CP in the Dark* potential given in Eq. (2.6) cannot be chosen arbitrarily. They have to be chosen such that the potential fulfills the theoretical requirement Boundedness From Below (BFB). This means that for arbitrarily large values of the scalar fields the potential always tends to $+\infty$ in every direction. For *CP in the Dark* the BFB condition is fulfilled if the couplings λ_{1-8} lie within the region given by [56]
$$\Omega_1 \cup \Omega_2 \quad , \tag{5.2}$$
where
$$\Omega_1 = \left\{ \lambda_1, \lambda_2, \lambda_6 > 0; \sqrt{\lambda_1\lambda_6} + \lambda_7 > 0; \sqrt{\lambda_2\lambda_6} + \lambda_8 > 0; \right.$$
$$\left. \sqrt{\lambda_1\lambda_2} + \lambda_3 + D > 0; \lambda_7 + \sqrt{\frac{\lambda_1}{\lambda_2}}\lambda_8 \geq 0 \right\} \quad , \tag{5.3}$$
$$\Omega_2 = \left\{ \lambda_1, \lambda_2, \lambda_6 > 0; \sqrt{\lambda_2\lambda_6} \geq \lambda_8 > -\sqrt{\lambda_2\lambda_6}; \sqrt{\lambda_1\lambda_6} > -\lambda_7 > \sqrt{\frac{\lambda_1}{\lambda_2}}\lambda_8; \right.$$
$$\left. \sqrt{(\lambda_7^2 - \lambda_1\lambda_6)(\lambda_8^2 - \lambda_2\lambda_6)} > \lambda_7\lambda_8 - (D + \lambda_3)\lambda_6 \right\} \tag{5.4}$$

and

$$D = \min(\lambda_4 - |\lambda_5|, 0) \quad . \tag{5.5}$$

The first condition from Ω_1 and Ω_2 restricts the free parameters λ_2 and λ_6 from (4.6) to be positive. However, the free parameter λ_8 is allowed to obtain negative values.

- The electroweak precision constraints S, T and U from Peskin-Takeuchi [57] on the scalar sector are also considered via the fit given in Ref. [58].

- `ScannerS` is linked to the codes `HiggsBounds`[59–62] and `HiggsSignals` [63, 64], which check for experimental constraints from LEP, Tevatron and LHC for extended scalar sectors. More precisely, these codes put constraints on additional Higgs particles predicted by any extended scalar sector model. `HiggsBounds` does this by comparing collision cross sections predicted by the additional Higgs particles of the model with the experimental exclusion limits of such collision cross sections obtained by LEP, Tevatron and LHC. `HiggsSignals` calculates the signal rates of the SM-like Higgs within the model and compares them with the signal rates of the measured Higgs boson from Tevatron and LHC. *CP in the Dark* introduces only one Higgs particle h, whose tree-level interactions and vertices are identical to the SM Higgs boson. In addition to that, m_{h_1} (and due to the mass ordering, $m_{h_{2/3}}$ as well) is chosen to be larger than 70 GeV and therefore larger than half the Higgs boson mass. This ensures that decays of the type $h \to h_i h_i$ do not occur and the decay widths of the Higgs boson remain identical to the SM values up to electroweak corrections with the exception of the diphoton decay. The diphoton decay will be treated in greater detail in Sec. 7.3.

- Since $H^\pm$ does not couple to fermions its interactions are not constrained by B-physics bounds. Furthermore, the LEP bound of $m_{H^\pm} > 90$ GeV due to decays of $H^\pm$ into fermions also does not need to be considered for the aforementioned reason. However, the mass of $H^\pm$ is chosen to be larger than the masses of h_2 and h_3 to avoid a charged DM candidate.

- The constraints coming from electric dipole moments [17, 18] do not need to be considered since all scalars, apart from the Higgs particle h, do not couple to fermions.

- To obtain the relic density from freeze-out the code `MicrOMEGAs` 5.3.41 [19, 49] is used. `ScannerS` imposes that the relic density calculated by `MicrOMEGAs` does not exceed
$$\Omega_{\text{model}} h^2 \leq \Omega_{\text{obs}} h^2 + 2\delta \quad , \tag{5.6}$$
where δ is the uncertainty given in Eq. (1.2). To make sure that `MicrOMEGAs` does not include h_1 in the thermal bath for its calculation it is moved to the list of feebly interactive particles via the internal function `defThermalset`. The freeze-in relic density will be calculated using a separate code developed in this thesis which is explained in detail in Chapter 6.

- In addition to the relic density, `MicrOMEGAs` also calculates the DM-nucleon scattering cross section. `ScannerS` uses this cross section to apply the DM-nucleon direct

	min.	max.
m_h	125.09 GeV	125.09 GeV
m_{h_1}	70 GeV	1000 GeV
m_{h_2}	70 GeV	1000 GeV
$m_{H^\pm}$	70 GeV	1000 GeV
α_1	$\pi/2$	$\pi/2$
α_2	$-\pi/2$	$\pi/2$
α_3	$-\pi/2$	$\pi/2$
λ_2	0	9
λ_6	0	17
λ_8	-10^{-10}	10^{-10}
m_{22}^2	0 GeV^2	10^6 GeV^2
m_S^2	$m_{h_1}^2 - 3 \cdot 10^{-7}\,\text{GeV}^2$	$m_{h_1}^2 + 3 \cdot 10^{-7}\,\text{GeV}^2$

Table 5.1.: `ScannerS` input parameter ranges for the free parameters of the model.

detection limits given by `XENON1T` [41]. This cross section is used to check for the direct detection constraints from the LZ experiment [42].

The parameter scan ranges of the free parameters chosen in (4.6) are listed in Tab. 5.1. All the DS particle masses are chosen such that the decays $h \to h_i h_i$ are kinematically forbidden. The scalar mixing angle $\alpha_1 = \pi/2$ ensures that h_1 freezes in (see Sec. 4.1), while α_2 and α_3 can vary between $-\pi/2$ and $\pi/2$. The couplings λ_2 and λ_6 are chosen at random in the intervals [0,9] and [0,17], respectively. The interval of the coupling λ_8, which represents the coupling between the DS particles which freeze-out and the freeze-in particle h_1, has to be chosen carefully. It has to be small enough, such that choosing a random λ_8 does not produce a relic density overabundance via the second term of Eq. (4.19), while simultaneously being large enough to be able to generate the observed relic density in Eq. (1.2). It is found that the interval $\left[-10^{-10}, 10^{-10}\right]$ fulfills this condition. Since λ_7 describes the coupling between the SM and h_1 it has to fulfill the same condition as λ_8 otherwise the first term of Eq. (4.19) will lead to an overabundance. However, λ_7 is not a free parameter, but is obtained from the free parameters via Eq. (4.7). This means that in order to obtain a small λ_7 coupling, m_S^2 has to be chosen such that $m_S^2 \approx m_{h_1}^2$. Therefore, m_S^2 is chosen to vary around $m_{h_1}^2$ in the interval $\left[m_{h_1}^2 - 3 \cdot 10^{-7}\,\text{GeV}^2, m_{h_1}^2 + 3 \cdot 10^{-7}\,\text{GeV}^2\right]$. The parameter m_{22}^2 is chosen randomly between 0 GeV^2 and 10^6 GeV^2.

6. Calculation of the Freeze-in Relic Density

The calculation of the freeze-in relic density is done via a code developed in this thesis using the computer algebra program `Mathematica` 12.00 [65]. To generate the tree-level diagrams needed for the $2 \to 2$ annihilation processes the package `FeynArts` [66] is used. With the package `FeynRules` [67] the model *CP in the Dark* is implemented into `FeynArts`. The diagrams are converted into algebraic expressions and simplified via the package `FeynCalc` [68].

The structure of the code can be subdivided into four separate steps. The first step is the generation of all tree-level $2 \to 2$ annihilation processes relevant for freeze-in and the calculation of their squared amplitude. In the second step these squared amplitudes are integrated over the phase space to obtain their cross sections. With these cross sections the TACs are calculated via Eq. (3.18) in the third step. In the last step the Boltzmann equation given in Eq. (4.19) is solved to obtain the yield Y_0 and with Eq. (3.31) the relic density generated via freeze-in.

6.1. Functions and Lists of the Code

The most important lists of the developed code are the following

- `SM` - the particle content of the SM with three identifiers for each particle
  - the `FeynArts` ID, for example F[3,{1}] for the up-quark,
  - an algebraic expression for the mass, i.e. *MU*
  - and a string ID, i.e. "u", which is capitalized for the anti-particle.
- `DS` - the particle content for the DS with the same identifiers as the SM.
- `FISMamp` - an empty list which is will be used to save the SM processes contributing to freeze-in, for example "$h1h1 \to ZZ$".
- `FIDSamp` - almost the same as the SM list above but with DS particles in the final states.
- `amp2lib` - a library that saves squared amplitudes and assigns them a unique key.

The auxiliary functions used are

- `createamp[process_]` - returns the amplitude for a given process ”$XY \to VZ$”. The diagrams for this amplitude are generated via `FeynArts` and put into an algebraic expression with `FeynCalc`.

- `amp22[process_]` - returns the algebraic expression of a tree level squared amplitude for a given $2 \to 2$ process. To save calculation time the squared amplitude is not calculated by directly multiplying the amplitude A (generated by `FeynArts`/`FeynCalc`) with its conjugate A^*. Instead A is broken down into the individual elements a_i made up of the expressions of the possible diagrams which contribute to the inserted process. For each element a_i the contributions to the squared amplitude are calculated by multiplication with another a_j. If $a_i = a_j$ the contribution to the squared amplitude is $|a_i|^2$. On the other hand, if $a_i \neq a_j$ the contribution becomes $2\text{Re}(a_i a_j^*)$. Each individual contribution is summed over their possible spins, polarizations and colors. Terms involving four momenta are written in terms of the Mandelstam variables s and t to allow for later integration over these variables. All contributions are summed up to give the total squared amplitude. The squared amplitude is multiplied by the correct spin, polarization and color factors. This approach gives compact tree-level squared amplitudes while simultaneously saving calculation time for processes with a large number of diagrams.

- `calccrs[amp2_,mi_,mj_,mk_,ml_]` - returns the cross section for the expression of a squared amplitude `amp2` with initial state masses $m_{i/j}$ and final state masses $m_{k/l}$ as defined in [69] in terms of the Mandelstam variable s. It is sufficient to give the expressions for the masses used in the SM/DS particle lists. Here the numerical values of the parameters obtained by `ScannerS` are substituted into the expression of `amp2` to save calculation time. The individual terms of the expression are integrated in parallel over the Mandelstam variable t to save more calculation time and are then summed up to give the cross section of `amp2`.

- `geff[T_]` - returns the effective degrees of freedom for the energy density at the thermal bath temperature T [GeV]. This is done by taking the data points given in Ref. [46] for $g_{\text{eff}}(T)$ and linearly interpolating between them. For temperatures larger than the maximum temperature of the data set, the maximum value of 106.75 is assumed.

- `heff[T_]` - returns the effective degrees of freedom for the entropy density at the thermal bath temperature T [GeV]. The same approach is done as with `geff[T_]`.

- `g12[T_]` - returns the value of the function defined in Eq. (3.27) at temperature T [GeV].

- `generatepoints[n_,lower_,upper_]` - generates `n` random logarithmically distributed points between the `lower` and `upper` bound. The endpoints are always included in the sample.

6.2. Relic Density Calculation Algorithm

To calculate the freeze-in relic density via Eq. (4.19), first all the amplitudes that contribute to the TACs $\langle\sigma v\rangle_{11X}$ and $\langle\sigma v\rangle_{11\mathrm{f}}$ have to be generated. The function

```
relevantamps[]
```

uses the particle content of the SM and the DS to calculate all the possible amplitudes. Here, it is important to note that not the whole SM is considered but only the Z, W and Higgs bosons as well as the top quark. This is due to the fact that all the amplitudes contributing to the final relic density either have a Higgs boson in the s-channel or (in the case of non fermionic initial/final states) a four point vertex between a DM particle pair and the SM particle pair. Since the coupling to the Higgs boson scales with the mass of the particles, only the four heaviest ones will be considered as the final state particles. By iterating over the SM and DS particle lists and inserting them as the final states into the function `createamp`, with the fixed initial state $h_1 h_1$, all possible $2 \to 2$ annihilation processes for freeze-in are generated. The processes that give non zero amplitudes are then saved in `FISMamp` for SM final states and `FIDSamp` for DS final states. Important to note is that only the name of the process (e.g. "$h1h1 \to Zh$") is saved not the amplitude itself.[1]

In the next step the function

```
loadscannerSdata[index_]
```

is called, which takes the parameter point at position `index` from `ScannerS` with all its constraints applied and assigns the randomly generated values to the model parameters.

From here the main computational part of the calculation begins. The function

```
createcrs[]
```

takes the list of all relevant $2 \to 2$ processes that contribute to freeze-in saved `FISMamp` and `FIDSamp` and goes through each element. When running the code for the first time it calculates for each process the squared amplitude via the function `amp22` and saves it in the library `amp2lib` with the name of process as the key. This library is then saved as .mx file such that the squared amplitudes can be accessed at any time. This means that when running this function multiple times, it first checks in `amp2lib` whether or not the squared amplitude has already been calculated and if it was, it just takes the algebraic expression from the library `amp2lib`. On the other hand, if it has not been calculated it calls

[1] Additionally, one might wonder why h_1 is in the initial state in all of these processes, if freeze-in describes the production of h_1 and is therefore expected to be in the final state. In the derivation of Eq. (3.3) it can be shown that both directions of the process $\chi\chi \leftrightarrow SM\,SM$ can be described by a single TAC in which the DM particles are in the initial state. Since Eq. (3.3) is used as a basis for all later derivations, this also applies to freeze-in.

the function `amp22` to calculate the squared amplitude and then saves it in the library with a unique key. Next, it plugs the squared amplitude into `calccrs` with the corresponding initial and final state masses to obtain the cross sections depending on s. Each cross section relevant for freeze-in is saved into the list `FISMcrs` for SM final states or `FIDScrs` for DS final states.

The cross sections are then used to calculate the TACs for each process with the function

`calctac[]`.

It uses the definition given in Eq. (3.18) for its calculation. First, 200 points are generated between 10^{-4} and 10 via the `generatepoints` function. These are the values of $x = m_{h_1}/T$ for which the TAC will be calculated. For each of these 200 x values the corresponding TAC is calculated numerically for every cross section determined in the previous step. To make sure that the integration region is well defined and real valued, the lower integration bound is chosen to be the squared rest mass of the heavier state between the initial and final state particles. The integration of Eq. (3.18) over s is done numerically using the `Mathematica` function `NIntegrate` for all 200 x values using the Trapezoidal integration method. This is again done in parallel for all cross sections. The numerical values of the TACs for each x are saved in a list. To obtain a function of the TAC which is defined at every x, the 200 x values and their corresponding TAC values are interpolated linearly. Increasing the number of randomly generated x increases the accuracy of the result by a maximum of $\sim 1\%$, while increasing the computation time significantly.

The last thing remaining, is to solve the Boltzmann equation in Eq. (4.19). For this, all the TACs with SM final states are added up into one function. The same is done for the TACs of the DS. The Boltzmann equation is then solved from $x = 10^{-4}$ to $x = 10$ with the initial condition $Y_1(10^{-4}) = 0$. This is done numerically using the explicit Runge Kutta method with the stiffness switching option of the `Mathematica` function `NDSolveValue`. The lower bound is chosen to give stable numerical results when solving the Boltzmann equation, while simultaneously saving computation time. Choosing a lower bound 1 order of magnitude lower does not change the result of the relic density, but increases computation time. However, choosing a lower bound which is larger by 1 order of magnitude leads to different results depending on the exact lower bound, making it numerically unstable. Although freeze-in ends at $x \approx 2-5$ [51] the upper bound is chosen to be $x = 10$ to make sure Y_1 reaches a constant value. The relic density contribution of h_1 is then given by

$$\Omega_1 h^2 = 2.742 \cdot 10^8 \frac{m_{h_1}}{\text{GeV}} Y_1(10) \quad . \tag{6.1}$$

The freeze-out relic density is calculated using the code `micrOMEGAs`.

The whole calculation is based on the non-relativistic approximation of the density distribution in Eq. (3.4). However, Fig. (6.1) shows the difference in relic density between using the Maxwell-Boltzmann distribution and the Fermi-Dirac/Bose-Einstein statistics for a real singlet scalar Higgs portal model. For masses of the DM candidate larger than half

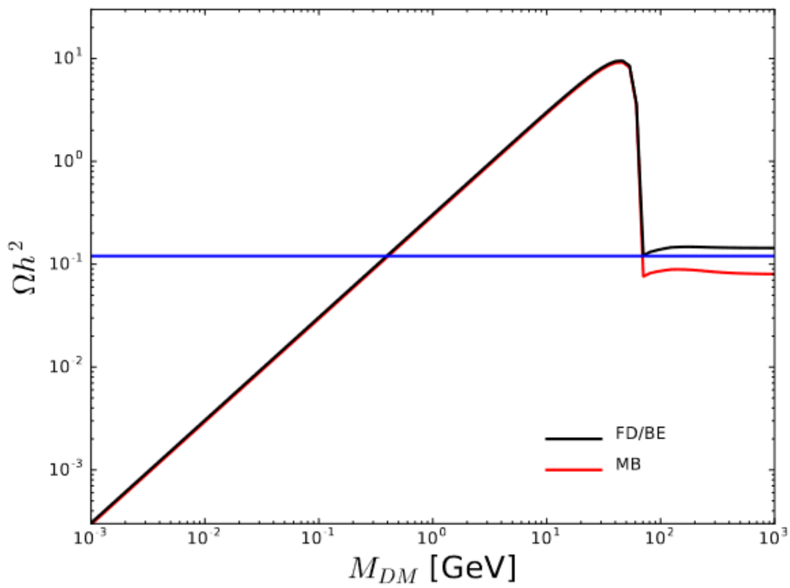

Figure 6.1.: Relic density generated via freeze-in over the mass of a singlet scalar DM candidate. The red line depicts the calculation with a Maxwell-Boltzmann (MB) distribution and the black line with a Fermi-Dirac/Bose-Einstein (FD/BE) distribution. The plot is taken from [49].

the Higgs boson mass they differ by a factor of two, while below they are identical. Since the freeze-in particle of *CP in the Dark* h_1 is also a real singlet where the only connection to the SM is via a Higgs portal and four points vertices, this additional factor of 2 is also considered in the calculation of the freeze-in relic density.

7. Results

In this chapter the numerical analysis on the investigations of this thesis will be presented. In Sec. 7.1 an analysis on the distribution of the relic density generated via freeze-in and freeze-out will be done. Section 7.2 discusses the consequences of the direct detection constraints on the viable parameter region. To investigate the influence of having an additional charged scalar in the model on the diphoton decay of the SM-like Higgs boson, Sec. 7.3 will compare its branching ratio with the SM value in the parameter space. To explain the features investigated in the previous sections, Sec. 7.4 will take a closer look at the part of the parameter space in which the relic density is mostly generated via freeze-out. In the following, unless stated differently, α_2 will always be chosen equal to $\pi/2$ such that the generation of the relic density is also possible via freeze-in.

7.1. Relic density

Figures 7.1 and 7.2 show the distribution of the parameter points which fulfill all constraints discussed in Ch. 5, where for the direct detection limit the limits given by `XENON1T` are taken into account. They are displayed in the plane of the full relic density

$$\Omega_{\text{full}}h^2 \equiv \Omega_{\text{f}}h^2 + \Omega_1 h^2 \quad , \tag{7.1}$$

where $\Omega_{\text{f}}h^2$ ($\Omega_1 h^2$) is the relic density generated via freeze-out (freeze-in) and of the masses m_{h_1} and $m_{h_{2/3}}$, respectively. The color coding shows the ratio between the relic density generated via freeze-in and the measured value given by Eq. (1.2). A value close to 1 corresponds to freeze-in being the main contributor to the full relic density, while small values mean that freeze-out is the main contributor. Throughout the whole mass spectrum of the scanned region it is possible to obtain the observed relic density. However, the parameter points which are able to generate the observed relic density are mostly dominated by the freeze-in mechanism. In the sample of N=23487 parameter points, 1 of the freeze-out-dominated points is able to generate the observed relic density within the 5σ bound of Eq. (1.2), while for the freeze-in-dominated points 412 are able to generate $\Omega_{\text{obs}}h^2$ within this bound. Here freeze-out (freeze-in) dominated points refer to the points in which freeze-out (freeze-in) contributes at least 95% to the full relic density in Eq. (7.1). In general, points that are close to the observed relic density for different masses are mostly dominated by freeze-in production. This can also be seen in Fig. 7.3, where the allowed parameter points are displayed in the plane of the full relic density and the ratio between the relic density generated via freeze-in and via freeze-out. A ration of $\Omega_1 h^2/\Omega_{\text{f}}h^2 > 1$ means that freeze-in contributes more than 50% to the full relic density, while for $\Omega_1 h^2/\Omega_{\text{f}}h^2 < 1$ freeze-out contributes more than 50% to the full relic density. Here, the correlation between the freeze-in contribution and the full relic density becomes

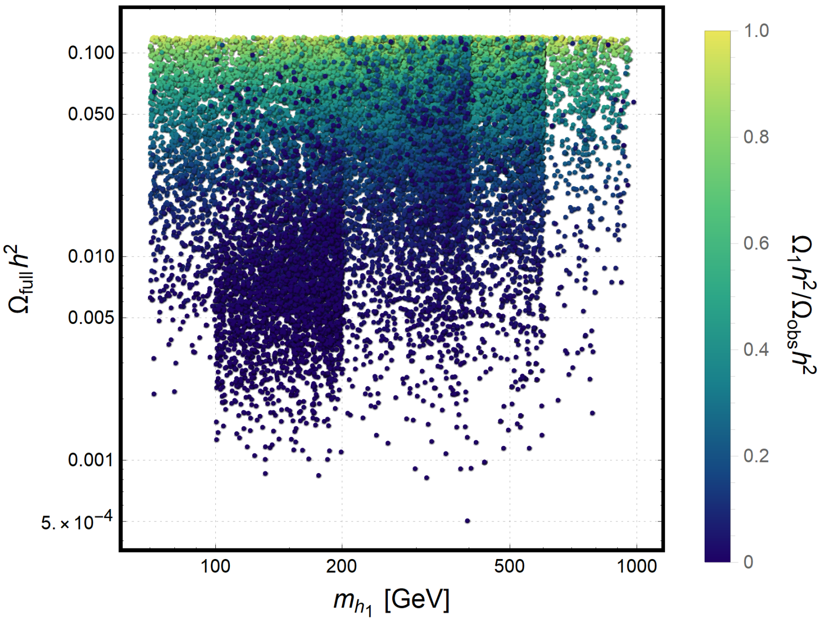

Figure 7.1.: Parameter points which pass the `ScannerS` and relic density constraints in the plane of the full relic density $\Omega_{\rm full}h^2$ and the mass of the freeze-in DM candidate m_{h_1}. The color coding shows the ratio between the relic density generated via freeze-in Ω_1 and the observed relic density $\Omega_{\rm obs}$.

more apparent. For most of the valid points, a large freeze-in contribution is necessary to obtain a large relic density as can be seen by the bulk of parameter points at $\Omega_{\rm full}h^2 \approx 0.12$ and $\Omega_1 h^2/\Omega_{\rm f}h^2 > 1$. Another important observation is the color gradient close to the $\Omega_{\rm full}h^2 = \Omega_{\rm obs}h^2 \approx 0.12$ value. It shows that points for which freeze-out starts to become more dominant, i.e. decreasing $\Omega_1 h^2/\Omega_{\rm f}h^2$, freeze-in is still crucial to obtain the full relic density. In other words, with the appropriate coupling strength, freeze-in is able to fill the gap between the relic density generated by freeze-out and the observed relic density.

7.2. Direct Detection

Figure 7.4 displays the effective spin-independent (SI) direct detection DM-Xenon cross section $\sigma_{\rm Xenon} \cdot f_{\chi\chi}$ versus the mass of the freeze-out DM candidate $m_{h_{2/3}}$ for parameter points which pass all the constraints. The color coding shows the value of the full relic density. The SI cross section is re-scaled with the normalized relic density to adjust for the underabundance of the freeze-out relic density,

$$\sigma_{\rm Xenon} \cdot f_{\chi\chi} \equiv \sigma_{\rm Xenon} \frac{\Omega_{\rm f}h^2}{\Omega_{\rm obs}h^2} \quad . \tag{7.2}$$

In order understand this, remark that in the experiment only the direct detection cross section between the freeze-out DM candidates $h_{2/3}$ and Xenon is considered and not between Xenon and h_1. Due to the low couplings required for freeze-in, the direct detection cross section of h_1-Xenon is many orders of magnitude smaller than the one of $h_{2/3}$-Xenon

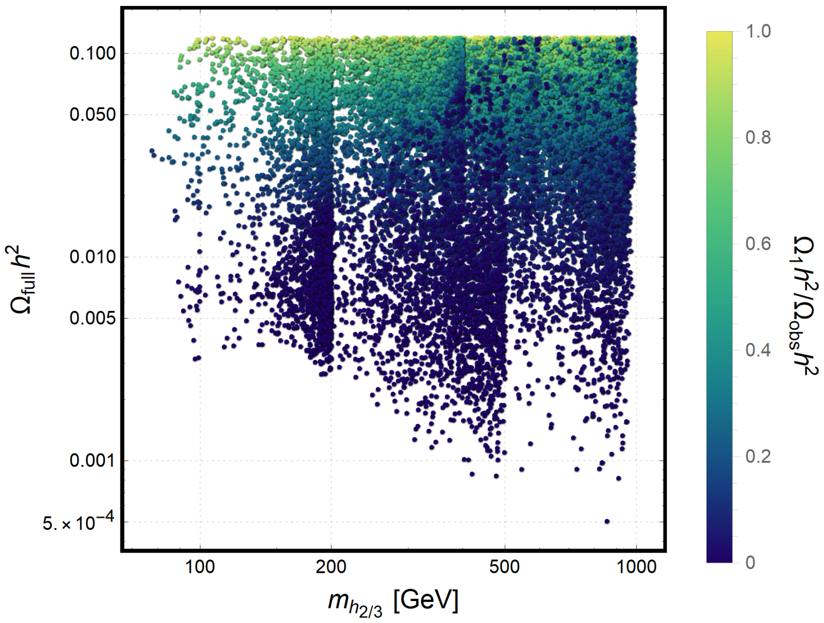

Figure 7.2.: Same as Fig. 7.1 but with the mass of the freeze-out DM candidates $m_{h_{2/3}}$ on the x-axis.

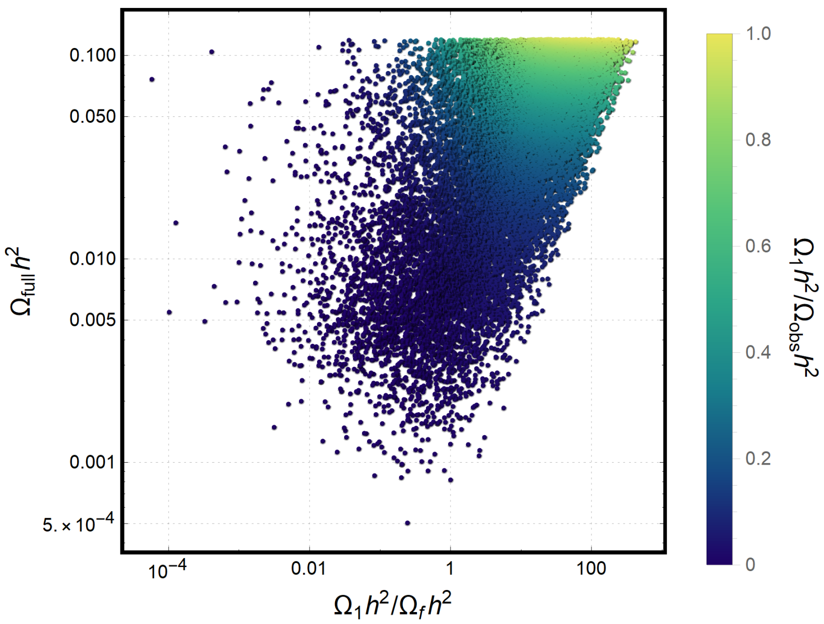

Figure 7.3.: Parameter points which pass the ScannerS and relic density constraints in the plane of the full relic density and the ratio of the relic density generated via freeze-in to the relic density generated via freeze-out. The color coding shows the ratio between the relic density generated via freeze-in and the observed relic density.

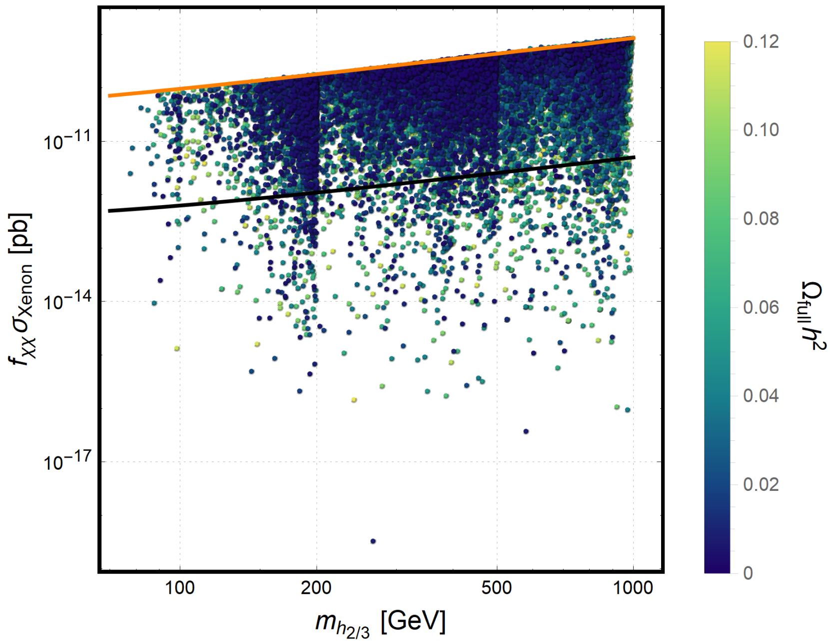

Figure 7.4.: The effective SI direct detection cross section over the DM mass $m_{h_{2/3}}$ for all points which pass the ScannerS and relic density constraints. The color coding shows the full relic density. The orange line represents the exclusion limit given by XENON1T [41] and the black line the neutrino floor [43].

and can therefore be neglected. As required by ScannerS, all points are below the XENON1T exclusion bound [41] . Additionally, the majority of the points are above the neutrino floor boundary represented by the black line. However, as already discussed in Sec. 2.4.2, the currently best bound on DM-Xenon direct detection is given by the LZ experiment [42]. By applying this additional bound Fig. 7.5 is obtained, where the LZ limit is represented by the red line. This still leaves a large amount of points in the region between the LZ limit and the neutrino floor, which can be tested by future DM direct detection experiments. In the following plots in this chapter the LZ bound is always considered. Further, points which are able to generate the observed relic density are spread throughout the whole allowed region. This implies that given the right freeze-in parameters it is possible to obtain the observed relic density for every allowed SI direct detection cross section. Figure 7.6 confirms this, by plotting the SI direct detection cross section over the full relic density. It shows that in the effective direct detection cross section range of $2.3 \cdot 10^{-10} - 10^{-15}$ pb the full relic density can be generated. As found in the previous section, most of the points which generate the full relic density are dominated by the freeze-in relic density as indicated by the color coding.

7.3. Diphoton Branching Ratio

The presence of an additional charged scalar in the model, i.e. $H^{\pm}$, changes the decay width of the SM-like Higgs boson into two photons. Along with the loops of the W boson

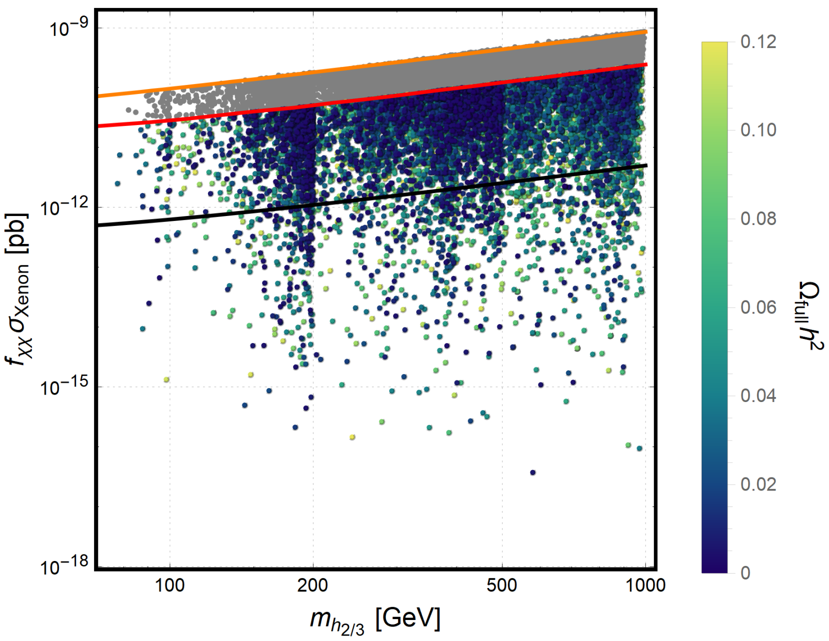

Figure 7.5.: Same as Fig. 7.4 but with the additional LZ bound [42] represented by the red line. The gray points are not allowed due to this bound.

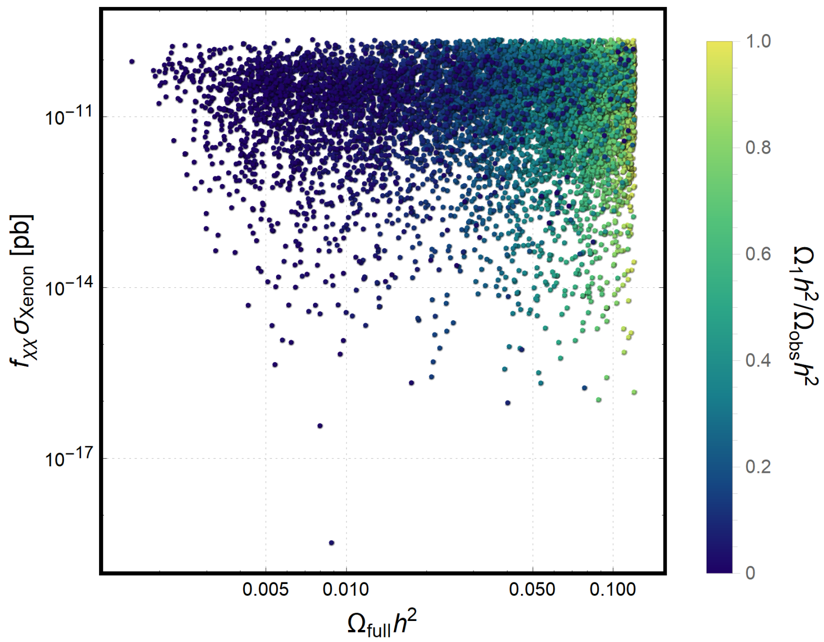

Figure 7.6.: The effective SI direct detection cross section over the full relic density for all points which pass all constraints including the LZ limit. The color coding shows the ratio between the relic density generated via freeze-in and the observed relic density.

and charged fermions, it introduces an additional $H^\pm$ loop into the decay width. Thus, the diphoton decay width of the SM-like Higgs boson h at leading order is given by [16]

$$\Gamma(h \to \gamma\gamma) = \frac{G_\mathrm{F}\alpha^2 m_h^3}{128\sqrt{2}\pi^3}\left|\sum_\mathrm{f} N_{\mathrm{c,f}} Q_\mathrm{f} A_{1/2}\left(\frac{4m_\mathrm{f}^2}{m_h^2}\right) + A_1\left(\frac{4m_W^2}{m_h^2}\right) + \frac{\lambda_3 v^2}{2m_{H^\pm}^2} A_0\left(\frac{4m_{H^\pm}^2}{m_h^2}\right)\right|^2 , \tag{7.3}$$

where G_F is the Fermi constant, α the fine-structure constant, $N_{\mathrm{c,f}}$ the color degrees of freedom of the fermion f, Q_f its charge and A_0, $A_{1/2}$ and A_1 the form factors for spin 0, 1/2, 1 particles, respectively. Their explicit form can be found in [70]. [1]

In Fig. 7.7 the branching ratio of the SM-like Higgs boson of the model normalized to the corresponding SM value is plotted for all allowed parameter points as a function of the charged Higgs mass $m_{H^\pm}$. The blue points fulfill all constraints (including the LZ-bound) while the green ones are overabundant when including freeze-in. Additionally, the current 2σ bounds on the normalized diphoton branching ratio by ATLAS [71] were applied[2],

$$\frac{\mathrm{BR}(h \to \gamma\gamma)}{\mathrm{BR}^\mathrm{SM}(h \to \gamma\gamma)} = 1.04^{+0.10}_{-0.09} , \tag{7.4}$$

which results in the lower bound of ~ 0.95.[3] Both types of points (the blue and the green ones) follow the same distribution. This means that the additional relic density generated via freeze-in does not influence the normalized diphoton branching ratio. This is expected since Eq. (7.3) does not depend on the parameters λ_7 and λ_8 which are relevant for freeze-in. However, due to the additional constraints obtained by setting $\alpha_2 = \pi/2$, the allowed parameter space changes when compared with the one, in which all DS particles freeze out. This can be seen by comparing Fig. 7.7 with Fig. 7.8, which is taken from Ref. [16] and which is based on a parameter sample where α_2 is not forced to be equal to $\pi/2$. The parameter space in the regime where all DS particles freeze out is much less constraint and therefore has a larger viable parameter space. This allows for points above ~ 1.01, which in the case of additional freeze-in would be excluded due to BFB and direct detection constraints because of setting $\alpha_2 = \pi/2$. Because of this, there is an observable that allows to differentiate between freeze-in and freeze-out, the rate into photons, given by $\sigma_\mathrm{prod}(h) \cdot \mathrm{BR}(h \to \gamma\gamma)$, where $\sigma_\mathrm{prod}(h)$ denotes the LHC production cross section of the SM-like Higgs boson and $\mathrm{BR}(h \to \gamma\gamma)$ its branching ratio into photons. Note, that since the production cross section in this model does not change w.r.t. the SM value, the rate is simply given by the branching ratio into photons. A measurement of normalized diphoton branching values above ~ 1.01 would rule out the freeze-in option. For points allowing for freeze-in, where hence $\alpha_2 = \pi/2$, it is possible to generate the observed relic density for every allowed normalized diphoton branching ratio. This can be seen in Fig. 7.9, where the parameter points are displayed in the plane of the ratio between the diphoton branching ratio of the SM-like Higgs boson normalized to its corresponding SM value and the full relic

[1] Note that the total width necessary for the computation of the branching ratio changes with respect to the SM total width only through the decay width into photons.

[2] This ATLAS constraint is also included in all previous and future plots.

[3] The bounds by CMS [72] were not considered since they would rule out the entire parameter space.

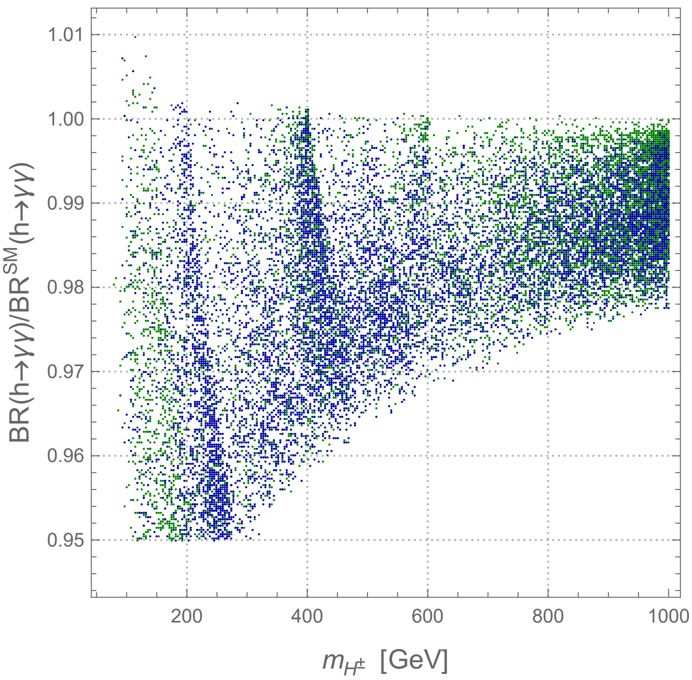

Figure 7.7.: Branching ratio of the SM-like Higgs boson h into two photons normalized to the corresponding SM value versus the mass of the charged scalar, $m_{H^\pm}$. The blue points pass all constraints including the LZ-bound. The green points fail the relic density constraint after taking freeze-in into account.

density. Again, most points that are able to achieve the observed relic density are freeze-in dominated as can be seen by the color bar. It can furthermore be observed that the freeze-out dominated points, that achieve the measured relic density, are not randomly distributed across the allowed branching ratios but are near the normalized diphoton branching ratio value of 1. This can nicely be inferred when plotting the relic density generated via freeze-out versus the diphoton branching ratio to its corresponding SM value, cf. Fig. 7.10. It can be seen that points achieving the full relic density through freeze-out have BR values close to the SM value. In contrast, for freeze-in dominated points achieving the observed relic density, the diphoton branching ratio can take values across the whole allowed value range.

Summarizing the discussion of this section it can be concluded: If it turns out that with future increased experimental precision the measured normalized diphoton branching ratio is found to be below one and if additionally it is assumed that the model is able to generate the full observed relic density, then the observed relic density is dominantly generated via freeze-in. This also gives insight in the parameter space region in which freeze-out is dominant as will be discussed in the next section.

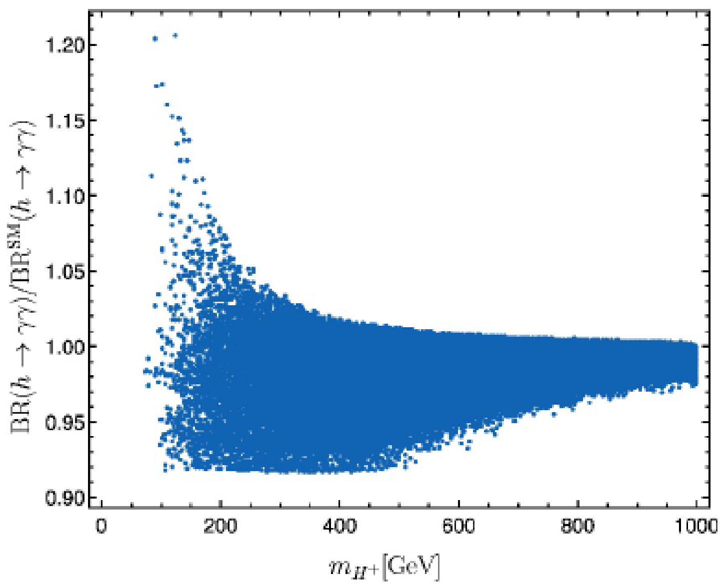

Figure 7.8.: Branching ratio of the SM-like Higgs boson h into two photons normalized to the corresponding SM value versus the mass of the charged scalar, $m_{H^{\pm}}$. The points pass all `ScannerS` constraints, however, here all DS particles freeze out. The plot is taken from [16].

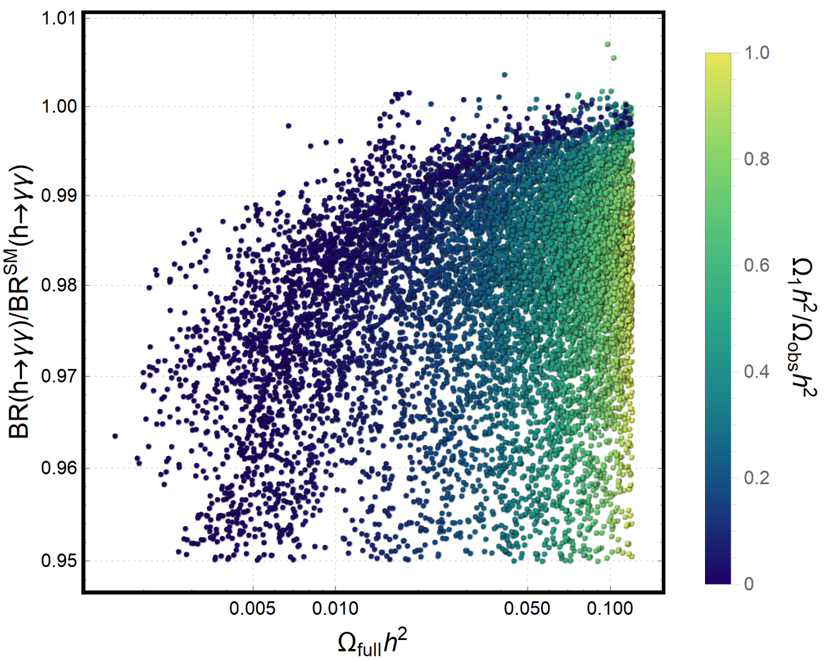

Figure 7.9.: Branching ratio of the SM-like Higgs boson h into two photons normalized to the corresponding SM value versus the full relic density. The parameter points pass all constraints including the LZ bound. The color coding shows the ratio between the relic density generated via freeze-in and the observed relic density.

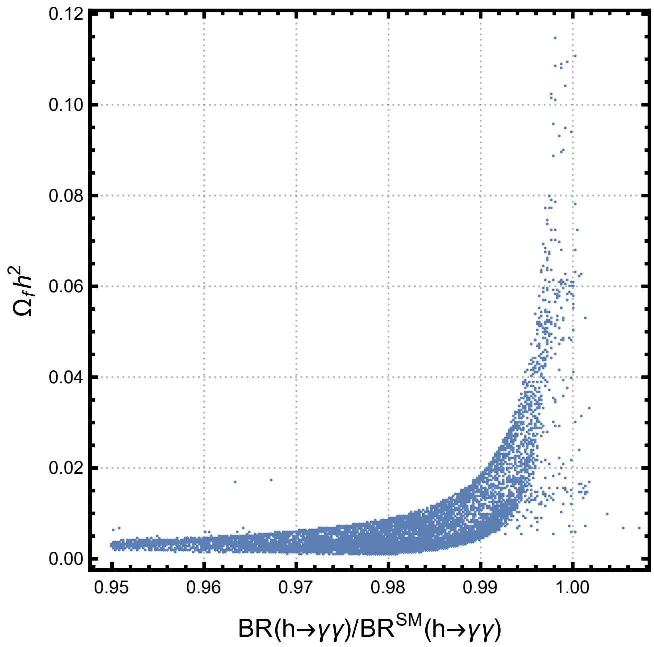

Figure 7.10.: Relic density generated via freeze-out versus the branching ratio of the SM-like Higgs boson h into two photons normalized to the corresponding SM value. The points pass all constraints.

7.4. Freeze-out Domination

As mentioned in the previous section there seems to be a specific parameter region in which freeze-out is dominant. The first step in finding out where this region in the parameter space lies, is by looking at Eq. (7.3) for the diphoton decay width and determining when it becomes close to the SM value. This is the case for small λ_3 couplings since then the additional contribution from the loop of the charged Higgs $H^{\pm}$ becomes negligible and only the two SM contributions to the diphoton decay width remain. Since freeze-out achieving the measured relic density value comes along with photonic decay widths close to the SM value, one of the conditions for a large freeze-out contribution is a small λ_3 which translates via Eq. (A.2) into the condition $m^2_{H^{\pm}} \approx m^2_{22}$.[4] The fact that λ_3 has to be small is an expected result since the coupling of the freeze-out DS particles ($h_{2/3}$ and $H^{\pm}$) to the SM particles involve Higgs portals and four-point vertices, whose couplings to the freeze-out particles are proportional to λ_3, as can be seen by Eqs. (A.10), (A.12), (A.15) and (A.17). Equations (A.10) and (A.15) also give the second condition for a high freeze-out contribution, namely that $\lambda_4 = -\lambda_3$. Setting $\alpha_2 = \pi/2$, as required in the sample, in Eq. (A.3) gives

$$\lambda_4 = \frac{(m^2_{h_2} + m^2_{h_3} - 2m^2_{H^{\pm}})}{v^2} = 2\frac{m^2_{h_{2/3}} - m^2_{H^{\pm}}}{v^2} \quad . \tag{7.5}$$

[4]One might think that a large value of $m_{H^{\pm}}$ also leads to a negligible loop contribution. However, when plugging in the definition of λ_3 from Eq. (A.2) the prefactor $\lambda_3 v^2/2m_{H^{\pm}}$ becomes $1 - m^2_{22}/m^2_{H^{\pm}}$. This leads to the condition $m^2_{22} \approx m^2_{H^{\pm}}$ for a small $H^{\pm}$ loop contribution, which is identical to the one needed for small λ_3.

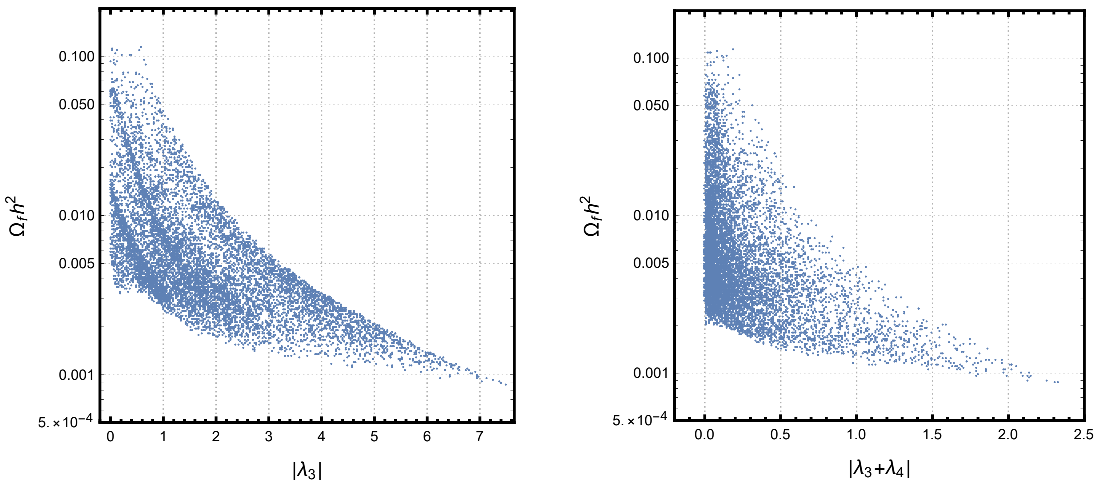

Figure 7.11.: Relic density generated via freeze-out over the absolute value of λ_3 (left) and $\lambda_3 + \lambda_4$ (right). The points pass all constraints.

Therefore, if λ_3 is small, the requirement for a small λ_4 is that $m_{h_{2/3}} \approx m_{H^\pm}$. The correlations between the freeze-out relic density and the absolute values of the couplings λ_3 and $\lambda_3 + \lambda_4$ are illustrated in Fig. 7.11. Here, the points which fulfill all constraints are plotted in the plane of the relic density generated via freeze-out and the absolute value of $|\lambda_3|$ (left) and $|\lambda_3 + \lambda_4|$ (right). The plots show that low values of $|\lambda_3|$ and $|\lambda_3 + \lambda_4|$ are not sufficient to guarantee a high freeze-out relic density. Even if both of these couplings are close to 0 a large portion of the points are still below the observed relic density. This is due to the couplings to the gauge bosons given in Eqs. (A.20), (A.23), (A.29) and (A.30). These couplings are independent of the free model parameters and therefore constant. This means that even if $\lambda_3 = \lambda_4 = 0$ the annihilation channels through the gauge bosons are still strong enough to provide efficient DM annihilation and hence a low freeze-out relic density. The third condition to obtain a large freeze-out relic density becomes apparent in Fig. 7.12. Here the relic density generated via freeze-out is plotted over the maximum between $|\lambda_3|$ and $|\lambda_3 + \lambda_4|$ for points which fulfill all constraints. The color gradient shows that a large mass of $h_{2/3}$ leads to a large relic density at every possible Max$(|\lambda_3|, |\lambda_3 + \lambda_4|)$-value. Going back to the definition of the TAC in Eq. (3.18) one can see why this is the case. The TAC is inversely proportional to the mass (even after integration over s) of the DM particle [51], which means that a large mass leads to a small TAC and therefore a large relic density. This leads to the three conditions for a large freeze-out relic density. They are a small λ_3, a small $\lambda_3 + \lambda_4$ and a large $m_{h_{2/3}}$. If these conditions are not fulfilled freeze-in is needed to generate the observed relic density.

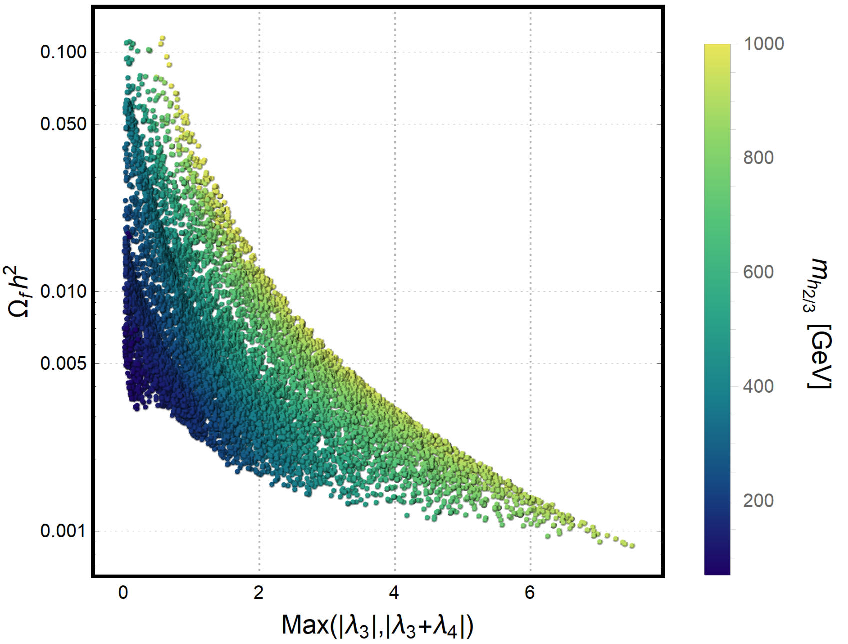

Figure 7.12.: Relic density generated via freeze-out over the maximum between $|\lambda_3|$ and $|\lambda_3 + \lambda_4|$. The points pass all constraints.

8. Conclusions

In this thesis, the possible DM generation mechanisms within the model *CP in the Dark*, freeze-in and freeze-out, were studied and their phenomenological implications were investigated. A code was developed to calculate the relic density via freeze-in. Even though the SM has a great success story, it leaves many questions unanswered in the field of particle physics. One of these questions is the nature of DM. The SM fails to provide a suitable DM candidate which is in agreement with the experimental data. This leads to the study of BSM theories which are able to provide one or more possible DM candidates, with *CP in the Dark* being one of those. *CP in the Dark* extends the scalar sector of the SM by an additional dark ($\mathbb{Z}_2$-odd) complex doublet field and a dark real singlet field. These fields introduce five DS particles into the model which are the three neutral scalars h_i ($i \in \{1, 2, 3\}$), with the mass hierarchy $m_{h_1} \leq m_{h_2} \leq m_{h_3}$, and two charged scalars $H^\pm$.

In Chapter 2, the model *CP in the Dark* was presented. The already mentioned DS particles were introduced and the CP violating properties of the model were shown. Since the additional CP violation only appears in the dark sector, constraints from electric dipole moments do need to be considered. Further, the three main experimental evidences for DM were presented and different methods of DM detection were discussed.

In the next chapter, an introduction of two mechanisms which thermally produce DM, namely freeze-out and freeze-in, were presented. The DM candidate in the first mechanism starts out in thermal equilibrium with the SM at the beginning of the universe and decouples from the SM bath at some point during its evolution to finally result in the currently observed relic density. A thorough derivation on how to obtain the relic density starting from the Boltzmann equations was given. The phenomenological aspect behind the differential equations describing freeze-out was discussed in detail. This was also done for the second mechanism freeze-in and compared with freeze-out. Lastly, the case of two DM candidates was discussed.

Since it already has been in shown in [16] that freeze-out is compatible with a large viable parameter space in *CP in the Dark*, Chapter 4 looked into the possibility of freeze-in in this model. There, it was shown that if the mixing angles, which diagonalize the Higgs mass matrix fulfill certain conditions, then the model produces three DM candidates among which two induce the relic density through freeze-out and one through freeze-in. The implications of this condition on the parameters space and the features of the model were discussed. Next, the Boltzmann equations for the particles that freeze-out and the particles that freeze-in were derived. These equations are used to calculate the relic density throughout the thesis.

In the next chapter all relevant experimental and theoretical constraints to obtain a viable parameter space were given. These constraints are checked via the code `ScannerS` and the code for the computation of the relic density through freeze-in, developed in this thesis. Freeze-out is checked through the link of `ScannerS` to `MicrOMEGAs`. Further, the scan intervals of the free parameters of the model were given.

The developed code, written in `Mathematica`, was described in detail in Chapter 6. This description includes the packages that were used, the lists and functions of the code and a thorough explanation of the algorithm that was used to calculate the relic density generated via freeze-in. The important assumption, which allows for a fast computation time, is that all particles follow a Maxwell-Boltzmann distribution. To adjust for the difference in relic density between using the Fermi-Dirac/Bose-Einstein and Maxwell-Boltzmann distribution, the results generated via the code are multiplied by a factor of 2, determined in Ref. [49].

In Chapter 7, the numerical analysis of this thesis was presented. In Sec. 7.1 it was shown that throughout the whole mass spectrum of the DM candidates the parameter sample can induce the observed relic density due to the freeze-in mechanism. Although the observed relic density can be obtained through a freeze-out dominated contribution, the parameter space in which freeze-in has a dominant contribution is much larger. The parameter space was investigated with respect to direct detection constraints in Sec. 7.2. Here, it was shown that parameter points are found which are below the direct detection limit set by the LZ experiment, while being above the neutrino floor. The observed relic density can be generated for parameter samples corresponding to a direct detection cross section which lies in the range of $2.3 \cdot 10^{-10} - 10^{-15}$ pb. In Sec. 7.3 the influence of an additional charged Higgs on the diphoton branching ratio of the SM-like Higgs boson was analyzed. It was shown that by imposing the mixing-angle condition necessary for freeze-in, a clear difference in the parameter space of the diphoton branching ratio of the SM-like Higgs boson normalized to the corresponding SM value emerges when compared to a scenario where this condition is not applied such that all DS particles freeze-out. This results in the fact that a measurement of the normalized diphoton branching ratio above ~ 1.01 rules out the freeze-in option. In the scenario where freeze-in is possible, this thesis was able to show that for a normalized diphoton branching ratio below one freeze-in is necessary to generate the full observed relic density. To understand why freeze-out of the particles $h_{2/3}$ and $H^{\pm}$ is able to generate the relic density only in the specific parameter region where the normalized diphoton branching ratio is close to one, Sec. 7.4 determined the conditions needed to obtain a large relic density via freeze-out.

In summary, *CP in the Dark* is able to generate the observed relic density via two mechanisms, namely freeze-in and freeze-out. The parameter region in which freeze-in is the main contributor to the observed relic density is much larger than the one for freeze-out. A possible next step would be to extend the model *CP in the Dark* such that it does not lose its CP violation property in the freeze-in scenario and therefore allows for the possibility of an SFOEWPT to explain the BAU while being able to generate the observed relic density.

A. Appendix

A.1. CP in the Dark Parameter Relations

CP in the Dark has 13 free parameters which define the model. The other 7 parameters can be obtained via the relations

$$m_{h_3}^2 = -\frac{m_{h_2}^2 R_{21} R_{22} + m_{h_1}^2 R_{11} R_{12}}{R_{31} R_{32}} \quad , \tag{A.1}$$

$$\lambda_3 = 2\frac{m_{H^\pm}^2 - m_{22}^2}{v^2} \quad , \tag{A.2}$$

$$\begin{aligned}\lambda_4 =& \frac{(m_{h_2}^2 + m_{h_3}^2 - 2m_{H^\pm}^2)(R_{13} - 2R_{21}R_{32}) + (m_{h_2}^2 - m_{h_1}^2)(2R_{12}R_{22}R_{23} + R_{13}R_{23}^2)}{v^2(R_{13} - 2R_{21}R_{32})} \\ &+ \frac{(m_{h_1}^2 - m_{h_3}^2)(2R_{12}R_{32}R_{33} + R_{13}R_{33}^2)}{v^2(R_{13} - 2R_{21}R_{32})} \quad ,\end{aligned} \tag{A.3}$$

$$\lambda_5 = \frac{R_{13}(m_{h_3}^2 - m_{h_1}^2 R_{23}^2 + m_{h_2}^2(R_{23}^2 - 1) + (m_{h_1}^2 - m_{h_3}^2)R_{33}^2)}{v^2(R_{13} - 2R_{21}R_{32})} \quad , \tag{A.4}$$

$$\begin{aligned}\lambda_7 =& -\frac{2(m_{h_2}^2 R_{23}(2R_{12}R_{22} + R_{13}R_{23}) + m_S^2(R_{13} - 2R_{21}R_{32}) + m_{h_3}^2(R_{11}R_{31} - R_{12}R_{32})R_{33})}{v^2(R_{13} - 2R_{21}R_{32})} \\ &+ \frac{2m_{h_1}^2(2R_{12}(R_{22}R_{23} - R_{32}R_{33}) + R_{13}(1 + R_{23}^2 - R_{33}^2) - 2R_{21}R_{32})}{v^2(R_{13} - 2R_{21}R_{32})} \quad ,\end{aligned} \tag{A.5}$$

$$\mathrm{Re}(A) = \frac{R_{11}((m_{h_2}^2 - m_{h_1}^2)R_{21}^2 + (m_{h_1}^2 - m_{h_3}^2)R_{31}^2)}{v^2(R_{13} - 2R_{21}R_{32})} \quad , \tag{A.6}$$

$$\mathrm{Im}(A) = \frac{R_{12}((m_{h_2}^2 - m_{h_1}^2)R_{21}^2 + (m_{h_1}^2 - m_{h_3}^2)R_{31}^2)}{v^2(R_{13} - 2R_{21}R_{32})} \quad , \tag{A.7}$$

where the matrix elements R_{ij} $(i, j = 1, 2, 3)$ of the neutral Higgs mixing matrix have been given in Eq. (2.13).

A.2. CP in the Dark Coupling Strengths in the Decoupling Limit

The coupling strengths λ between the DS and the SM particles, as well as the DS self-interactions, in the limit $\alpha_2 = \pi/2$ are given in terms of the *CP in the Dark* parameters and the electric coupling e as well as the Weinberg angle θ_W $(i, j = 1, 2, 3)$

$$\lambda(h, h_1, h_1) = -iv\lambda_7 \tag{A.8}$$
$$\lambda(h, h_1, h_2) = \lambda(h, h_1, h_3) = 0 \tag{A.9}$$
$$\lambda(h, h_2, h_2) = \lambda(h, h_3, h_3) = -iv(\lambda_3 + \lambda_4) \tag{A.10}$$
$$\lambda(h, h_2, h_3) = 0 \tag{A.11}$$
$$\lambda(h, H^+, H^-) = -iv\lambda_3 \tag{A.12}$$
$$\lambda(h, h, h_1, h_1) = -i\lambda_7 \tag{A.13}$$
$$\lambda(h, h, h_1, h_2) = \lambda(h, h, h_1, h_3) = 0 \tag{A.14}$$
$$\lambda(h, h, h_2, h_2) = \lambda(h, h, h_3, h_3) = -i(\lambda_3 + \lambda_4) \tag{A.15}$$
$$\lambda(h, h, h_2, h_3) = 0 \tag{A.16}$$
$$\lambda(h, h, H^+, H^-) = -i\lambda_3 \tag{A.17}$$
$$\lambda(Z, h_i, h_i) = 0 \tag{A.18}$$
$$\lambda(Z, h_1, h_2) = \lambda(Z, h_1, h_3) = 0 \tag{A.19}$$
$$\lambda(Z, h_2, h_3) = -\frac{e}{2\cos\theta_W \sin\theta_W} \tag{A.20}$$
$$\lambda(Z, Z, h_i, h_j) = 0 \ , \quad (i \neq j) \tag{A.21}$$
$$\lambda(Z, Z, h_1, h_1) = 0 \tag{A.22}$$
$$\lambda(Z, Z, h_2, h_2) = \lambda(Z, Z, h_3, h_3) = i\frac{e^2}{2\cos^2\theta_W \sin^2\theta_W} \tag{A.23}$$
$$\lambda(W^+, h_1, H^-) = 0 \tag{A.24}$$
$$\lambda(W^+, h_2, H^-) = -e\frac{\cos(\alpha_1 + \alpha_3) + i\sin(\alpha_1 + \alpha_3)}{2\sin\theta_W} \tag{A.25}$$
$$\lambda(W^+, h_3, H^-) = -e\frac{i\cos(\alpha_1 + \alpha_3) - \sin(\alpha_1 + \alpha_3)}{2\sin\theta_W} \tag{A.26}$$
$$\lambda(W^+, W^-, h_1, h_i) = 0 \tag{A.27}$$
$$\lambda(W^+, W^-, h_2, h_3) = 0 \tag{A.28}$$
$$\lambda(W^+, W^-, h_2, h_2) = \lambda(W, W, h_3, h_3) = i\frac{e^2}{2\sin^2\theta_W} \tag{A.29}$$
$$\lambda(W^+, W^-, H^+, H^-) = i\frac{e^2}{2\sin^2\theta_W} \tag{A.30}$$
$$\tag{A.31}$$

$$\lambda(h_1,h_1,h_1,h_1) = -3i\lambda_6 \tag{A.32}$$

$$\lambda(h_2,h_2,h_2,h_2) = \lambda(h_3,h_3,h_3,h_3) = -3i\lambda_2 \tag{A.33}$$

$$\lambda(h_1,h_1,h_2,h_2) = \lambda(h_1,h_1,h_3,h_3) = -i\lambda_8 \tag{A.34}$$

$$\lambda(h_2,h_2,h_3,h_3) = -i\lambda_2 \tag{A.35}$$

$$\lambda(h_i,h_j,h_k,h_l) = 0 \ , \quad (i \neq j,k,l) \tag{A.36}$$

$$\lambda(H^+,H^-,h_1,h_1) = -i\lambda_8 \tag{A.37}$$

$$\lambda(H^+,H^-,h_2,h_2) = \lambda(H^+,H^-,h_3,h_3) = -i\lambda_2 \tag{A.38}$$

$$\lambda(H^+,H^-,h_i,h_j) = 0 \ , \quad (i \neq j) \tag{A.39}$$

Acknowledgements

I would like to sincerely thank Prof. Dr. Milada Margarete Mühlleitner for providing me with this opportunity to work on such a fascinating topic. I thoroughly enjoyed our weekly meetings in which we had many fruitful discussions and new ideas were always welcomed. Thanks for enabling me to attend an exceptionally interesting summer school and to visit our collaborators in Portugal. Thanks for guiding me through the first steps of what will hopefully be a long career in the field of Theoretical Physics.

Thanks a lot to PD Dr. Stefan Gieseke for agreeing to be the second reviewer of this thesis.

I would also like to thank Prof. Dr. Rui Santos for helping me to formulate my thoughts and asking questions which allowed me to deepen my understanding of this topic. It was always a pleasure to have him in our weekly meetings.

Thanks to Dr. Duarte Azevedo for always patiently answering my questions regarding *CP in the Dark* and proof reading my thesis.

Thanks to my project colleagues M.Sc. Rodrigo Capucha and B.Sc. (soon M.Sc.) Karim Elyaouti. We had a great group dynamic which allowed us to progress fast and solve problems efficiently. I am looking forward to work with them on future projects.

Thanks to M.Sc. Lisa Biermann for helping me out with all my IT problems and administrating the ITP infrastructure.

Last but not least, thanks to my office partner M.Sc. Felix Egle with whom I could always chat about Physics related and Physics unrelated topics.

Bibliography

[1] G. Aad et al. "Observation of a new particle in the search for the Standard Model Higgs boson with the ATLAS detector at the LHC". In: *Physics Letters B* 716.1 (Sept. 2012), pp. 1–29. DOI: 10.1016/j.physletb.2012.08.020. URL: https://doi.org/10.1016%2Fj.physletb.2012.08.020.

[2] S. Chatrchyan et al. "Observation of a new boson at a mass of 125 GeV with the CMS experiment at the LHC". In: *Physics Letters B* 716.1 (Sept. 2012), pp. 30–61. DOI: 10.1016/j.physletb.2012.08.021. URL: https://doi.org/10.1016%2Fj.physletb.2012.08.021.

[3] Georges Aad et al. "Combined Measurement of the Higgs Boson Mass in pp Collisions at $\sqrt{s} = 7$ and 8 TeV with the ATLAS and CMS Experiments". In: *Phys. Rev. Lett.* 114 (2015), p. 191803. DOI: 10.1103/PhysRevLett.114.191803. arXiv: 1503.07589 [hep-ex].

[4] STEPHEN P. MARTIN. "A SUPERSYMMETRY PRIMER". In: *Perspectives on Supersymmetry*. WORLD SCIENTIFIC, July 1998, pp. 1–98. DOI: 10.1142/9789812839657_0001. URL: https://doi.org/10.1142%2F9789812839657_0001.

[5] Howard E. Haber and Laurel Stephenson Haskins. "Supersymmetric Theory and Models". In: *Anticipating the Next Discoveries in Particle Physics*. WORLD SCIENTIFIC, May 2018. DOI: 10.1142/9789813233348_0006. URL: https://doi.org/10.1142%2F9789813233348_0006.

[6] C. L. Bennett et al. "Nine-Year Wilkinson Microwave Anisotropy Probe (WMAP) Observations: Final Maps and Results". In: *Astrophys. J. Suppl.* 208 (2013), p. 20. DOI: 10.1088/0067-0049/208/2/20. arXiv: 1212.5225 [astro-ph.CO].

[7] N. Aghanim et al. "iPlanck/i2018 results". In: *Astronomy &amp Astrophysics* 641 (Sept. 2020), A6. DOI: 10.1051/0004-6361/201833910. URL: https://doi.org/10.1051%2F0004-6361%2F201833910.

[8] A. D. Sakharov. "Violation of CP Invariance, C asymmetry, and baryon asymmetry of the universe". In: *Pisma Zh. Eksp. Teor. Fiz.* 5 (1967), pp. 32–35. DOI: 10.1070/PU1991v034n05ABEH002497.

[9] James M. Cline. *Baryogenesis*. 2006. DOI: 10.48550/ARXIV.HEP-PH/0609145. URL: https://arxiv.org/abs/hep-ph/0609145.

[10] F. Csikor, Z. Fodor, and J. Heitger. "End Point of the Hot Electroweak Phase Transition". In: *Physical Review Letters* 82.1 (Jan. 1999), pp. 21–24. DOI: 10.1103/physrevlett.82.21. URL: https://doi.org/10.1103%2Fphysrevlett.82.21.

[11] K. Kajantie et al. “Is There a Hot Electroweak Phase Transition at $m_H m_W$”. In: *Physical Review Letters* 77.14 (Sept. 1996), pp. 2887–2890. DOI: 10.1103/physrevlett.77.2887. URL: https://doi.org/10.1103%2Fphysrevlett.77.2887.

[12] A.G. Doroshkevich, Vladimir N. Lukash, and E.V. Mikheeva. “A solution to the problems of cusps and rotation curves in dark matter halos in the cosmological standard model”. In: *Uspekhi Fizicheskih Nauk* 182.1 (2012), p. 3. DOI: 10.3367/ufnr.0182.201201a.0003. URL: https://doi.org/10.3367%2Fufnr.0182.201201a.0003.

[13] Federico Lelli et al. “One Law to Rule Them All: The Radial Acceleration Relation of Galaxies”. In: *The Astrophysical Journal* 836.2 (Feb. 2017), p. 152. DOI: 10.3847/1538-4357/836/2/152. URL: https://doi.org/10.3847%2F1538-4357%2F836%2F2%2F152.

[14] Yoshiaki Sofue. *Rotation Curve of the Milky Way and the Dark Matter Density*. 2020. DOI: 10.48550/ARXIV.2004.11688. URL: https://arxiv.org/abs/2004.11688.

[15] Douglas Clowe et al. “A Direct Empirical Proof of the Existence of Dark Matter”. In: *The Astrophysical Journal* 648.2 (Aug. 2006), pp. L109–L113. DOI: 10.1086/508162. URL: https://doi.org/10.1086%2F508162.

[16] Duarte Azevedo et al. “CP in the dark”. In: *Journal of High Energy Physics* 2018.11 (Nov. 2018). DOI: 10.1007/jhep11(2018)091. URL: https://doi.org/10.1007%2Fjhep11%282018%29091.

[17] V. et al. Andreev. “Improved limit on the electric dipole moment of the electron”. In: *Nature* 562 (Oct. 2018). DOI: 10.1103/s41586-018-0599-8. URL: https://doi.org/10.1038%s41586-018-0599-8.

[18] J.W. Martin. “Current status of neutron electric dipole moment experiments”. In: *Journal of Physics: Conference Series* 1643.1 (Dec. 2020), p. 012002. DOI: 10.1088/1742-6596/1643/1/012002. URL: https://dx.doi.org/10.1088/1742-6596/1643/1/012002.

[19] G. Bélanger et al. “micrOMEGAs_3: A program for calculating dark matter observables”. In: *Computer Physics Communications* 185.3 (Mar. 2014), pp. 960–985. DOI: 10.1016/j.cpc.2013.10.016. URL: https://doi.org/10.1016%2Fj.cpc.2013.10.016.

[20] Rita Coimbra, Marco O. P. Sampaio, and Rui Santos. “ScannerS: constraining the phase diagram of a complex scalar singlet at the LHC”. In: *The European Physical Journal C* 73.5 (May 2013). DOI: 10.1140/epjc/s10052-013-2428-4. URL: https://doi.org/10.1140%2Fepjc%2Fs10052-013-2428-4.

[21] Margarete Mühlleitner et al. *ScannerS: Parameter Scans in Extended Scalar Sectors*. 2020. DOI: 10.48550/ARXIV.2007.02985. URL: https://arxiv.org/abs/2007.02985.

[22] Michael E. Peskin and Daniel V. Schroeder. *An Introduction to quantum field theory*. Reading, USA: Addison-Wesley, 1995. ISBN: 978-0-201-50397-5.

[23] P.W. Higgs. “Broken symmetries, massless particles and gauge fields”. In: *Physics Letters* 12.2 (Sept. 1964), pp. 132–133. DOI: 10.1016/0031-9163(64)91136-9.

[24] F. Englert and R. Brout. “Broken Symmetry and the Mass of Gauge Vector Mesons”. In: *Physical Review Letters* 13.9 (Aug. 1964), pp. 321–323. DOI: 10.1103/physrevlett.13.321.

[25] Jeffrey Goldstone, Abdus Salam, and Steven Weinberg. "Broken Symmetries". In: *Phys. Rev.* 127 (3 Aug. 1962), pp. 965–970. DOI: 10.1103/PhysRev.127.965. URL: https://link.aps.org/doi/10.1103/PhysRev.127.965.

[26] Georges Aad et al. "Observation of a new particle in the search for the Standard Model Higgs boson with the ATLAS detector at the LHC". In: *Phys. Lett.* B716 (2012), pp. 1–29. DOI: 10.1016/j.physletb.2012.08.020. arXiv: 1207.7214 [hep-ex].

[27] Serguei Chatrchyan et al. "Observation of a new boson at a mass of 125 GeV with the CMS experiment at the LHC". In: *Phys. Lett.* B716 (2012), pp. 30–61. DOI: 10.1016/j.physletb.2012.08.021. arXiv: 1207.7235 [hep-ex].

[28] Timothy Clifton et al. "Modified gravity and cosmology". In: *Physics Reports* 513.1-3 (Mar. 2012), pp. 1–189. DOI: 10.1016/j.physrep.2012.01.001. URL: https://doi.org/10.1016%2Fj.physrep.2012.01.001.

[29] Bernard Carr and Florian Kühnel. "Primordial black holes as dark matter candidates". In: *SciPost Physics Lecture Notes* (May 2022). DOI: 10.21468/scipostphyslectnotes.48. URL: https://doi.org/10.21468%2Fscipostphyslectnotes.48.

[30] K. Freese. "Review of Observational Evidence for Dark Matter in the Universe and in upcoming searches for Dark Stars". In: *EAS Publications Series* 36 (2009), pp. 113–126. DOI: 10.1051/eas/0936016. URL: https://doi.org/10.1051%2Feas%2F0936016.

[31] D. J. Fixsen. "THE TEMPERATURE OF THE COSMIC MICROWAVE BACKGROUND". In: *The Astrophysical Journal* 707.2 (Nov. 2009), p. 916. DOI: 10.1088/0004-637X/707/2/916. URL: https://dx.doi.org/10.1088/0004-637X/707/2/916.

[32] Martin Bauer and Tilman Plehn. *Yet Another Introduction to Dark Matter.* 2017. DOI: 10.48550/ARXIV.1705.01987. URL: https://arxiv.org/abs/1705.01987.

[33] N. Aghanim et al. "iPlanck/i2015 results". In: *Astronomy &amp Astrophysics* 594 (Sept. 2016), A11. DOI: 10.1051/0004-6361/201526926. URL: https://doi.org/10.1051%2F0004-6361%2F201526926.

[34] R. D. Peccei. "QCD, Strong CP and Axions". In: (1996). DOI: 10.48550/ARXIV.HEP-PH/9606475. URL: https://arxiv.org/abs/hep-ph/9606475.

[35] R. Khatiwada et al. "Axion Dark Matter Experiment: Detailed design and operations". In: *Review of Scientific Instruments* 92.12 (Dec. 2021), p. 124502. DOI: 10.1063/5.0037857. URL: https://doi.org/10.1063%2F5.0037857.

[36] Katharina-Sophie Isleif and. "The Any Light Particle Search Experiment at DESY". In: *Moscow University Physics Bulletin* 77.2 (Apr. 2022), pp. 120–125. DOI: 10.3103/s002713492202045x. URL: https://doi.org/10.3103%2Fs002713492202045x.

[37] F. J. Iguaz. "The CAST experiment: status and perspectives". In: (2011). DOI: 10.48550/ARXIV.1110.2116. URL: https://arxiv.org/abs/1110.2116.

[38] M. Ajello et al. "iFERMI/i-LAT OBSERVATIONS OF HIGH-ENERGYiγ/i-RAY EMISSION TOWARD THE GALACTIC CENTER". In: *The Astrophysical Journal* 819.1 (Feb. 2016), p. 44. DOI: 10.3847/0004-637x/819/1/44. URL: https://doi.org/10.3847%2F0004-637x%2F819%2F1%2F44.

[39] Kevork N Abazajian. "The consistency of Fermi-LAT observations of the galactic center with a millisecond pulsar population in the central stellar cluster". In: *Journal of Cosmology and Astroparticle Physics* 2011.03 (Mar. 2011), pp. 010–010. DOI: 10.1088/1475-7516/2011/03/010. URL: https://doi.org/10.1088%2F1475-7516%2F2011%2F03%2F010.

[40] D. G. Cerdeñ o and A. M. Green. "Direct detection of WIMPs". In: *Particle Dark Matter*. Cambridge University Press, Jan. 2010, pp. 347–369. DOI: 10.1017/cbo9780511770739.018. URL: https://doi.org/10.1017%2Fcbo9780511770739.018.

[41] E. Aprile et al. "Dark Matter Search Results from a One Ton-Year Exposure of XENON1T". In: *Physical Review Letters* 121.11 (Sept. 2018). DOI: 10.1103/physrevlett.121.111302. URL: https://doi.org/10.1103%2Fphysrevlett.121.111302.

[42] J. et al Aalbers. *First Dark Matter Search Results from the LUX-ZEPLIN (LZ) Experiment*. 2022. DOI: 10.48550/ARXIV.2207.03764. URL: https://arxiv.org/abs/2207.03764.

[43] Ciaran A. J. O'Hare. "New Definition of the Neutrino Floor for Direct Dark Matter Searches". In: *Physical Review Letters* 127.25 (Dec. 2021). DOI: 10.1103/physrevlett.127.251802. URL: https://doi.org/10.1103%2Fphysrevlett.127.251802.

[44] G. Aad et al. "Search for invisible Higgs-boson decays in events with vector-boson fusion signatures using 139 fb-1 of proton-proton data recorded by the ATLAS experiment". In: *Journal of High Energy Physics* 2022.8 (Aug. 2022). DOI: 10.1007/jhep08(2022)104. URL: https://doi.org/10.1007%2Fjhep08%282022%29104.

[45] Paolo Gondolo and Graciela Gelmini. "Cosmic abundances of stable particles: Improved analysis". In: *Nuclear Physics B* 360.1 (1991), pp. 145–179. ISSN: 0550-3213. DOI: https://doi.org/10.1016/0550-3213(91)90438-4. URL: https://www.sciencedirect.com/science/article/pii/0550321391904384.

[46] Lars Husdal. "On Effective Degrees of Freedom in the Early Universe". In: *arXiv: Cosmology and Nongalactic Astrophysics* 4 (2016), p. 78.

[47] Joakim Edsjö and Paolo Gondolo. "Neutralino relic density including coannihilations". In: *Physical Review D* 56.4 (Aug. 1997), pp. 1879–1894. DOI: 10.1103/physrevd.56.1879. URL: https://doi.org/10.1103%2Fphysrevd.56.1879.

[48] Milton Abramowitz and Irene A. Stegun. *Handbook of mathematical functions with formulas, graphs and mathematical tables*. English. Washington: U.S. Department of Commerce. xiv, 1046 pp. (1964). 1964.

[49] G. Bélanger et al. "micrOMEGAs5.0 : Freeze-in". In: *Computer Physics Communications* 231 (Oct. 2018), pp. 173–186. DOI: 10.1016/j.cpc.2018.04.027. URL: https://doi.org/10.1016%2Fj.cpc.2018.04.027.

[50] Yong Du et al. "Revisiting dark matter freeze-in and freeze-out through phase-space distribution". In: *Journal of Cosmology and Astroparticle Physics* 2022.04 (Apr. 2022), p. 012. DOI: 10.1088/1475-7516/2022/04/012. URL: https://doi.org/10.1088%2F1475-7516%2F2022%2F04%2F012.

[51] Lawrence J. Hall et al. “Freeze-in production of FIMP dark matter”. In: *Journal of High Energy Physics* 2010.3 (Mar. 2010). DOI: 10.1007/jhep03(2010)080. URL: https://doi.org/10.1007%2Fjhep03%282010%29080.

[52] Genevi è ve Bélanger and Jong-Chul Park. “Assisted freeze-out”. In: *Journal of Cosmology and Astroparticle Physics* 2012.03 (Mar. 2012), pp. 038–038. DOI: 10.1088/1475-7516/2012/03/038. URL: https://doi.org/10.1088%2F1475-7516%2F2012%2F03%2F038.

[53] Gaël Alguero et al. “Co-scattering in micrOMEGAs: A case study for the singlet-triplet dark matter model”. In: *SciPost Physics* 13.6 (Dec. 2022). DOI: 10.21468/scipostphys.13.6.124. URL: https://doi.org/10.21468%2Fscipostphys.13.6.124.

[54] Carl M. Bender and Sarben Sarkar. “Asymptotic analysis of the Boltzmann equation for dark matter relics”. In: *Journal of Mathematical Physics* 53.10 (Oct. 2012), p. 103509. DOI: 10.1063/1.4753990. URL: https://doi.org/10.1063%2F1.4753990.

[55] I. F. Ginzburg and I. P. Ivanov. “Tree-level unitarity constraints in the most general two Higgs doublet model”. In: *Physical Review D* 72.11 (Dec. 2005). DOI: 10.1103/physrevd.72.115010. URL: https://doi.org/10.1103%2Fphysrevd.72.115010.

[56] Margarete Mühlleitner et al. “The N2HDM under theoretical and experimental scrutiny”. In: *Journal of High Energy Physics* 2017.3 (Mar. 2017). DOI: 10.1007/jhep03(2017)094. URL: https://doi.org/10.1007%2Fjhep03%282017%29094.

[57] Michael E. Peskin and Tatsu Takeuchi. “Estimation of oblique electroweak corrections”. In: *Phys. Rev. D* 46 (1 July 1992), pp. 381–409. DOI: 10.1103/PhysRevD.46.381. URL: https://link.aps.org/doi/10.1103/PhysRevD.46.381.

[58] J. Haller et al. “Update of the global electroweak fit and constraints on two-Higgs-doublet models”. In: *The European Physical Journal C* 78.8 (Aug. 2018). DOI: 10.1140/epjc/s10052-018-6131-3. URL: https://doi.org/10.1140%2Fepjc%2Fs10052-018-6131-3.

[59] P. Bechtle et al. “HiggsBounds: Confronting arbitrary Higgs sectors with exclusion bounds from LEP and the Tevatron”. In: *Computer Physics Communications* 181.1 (Jan. 2010), pp. 138–167. DOI: 10.1016/j.cpc.2009.09.003. URL: https://doi.org/10.1016%2Fj.cpc.2009.09.003.

[60] P. Bechtle et al. “HiggsBounds 2.0.0: Confronting neutral and charged Higgs sector predictions with exclusion bounds from LEP and the Tevatron”. In: *Computer Physics Communications* 182.12 (Dec. 2011), pp. 2605–2631. DOI: 10.1016/j.cpc.2011.07.015. URL: https://doi.org/10.1016%2Fj.cpc.2011.07.015.

[61] Philip Bechtle et al. *Recent Developments in HiggsBounds and a Preview of HiggsSignals*. 2013. DOI: 10.48550/ARXIV.1301.2345. URL: https://arxiv.org/abs/1301.2345.

[62] Philip Bechtle et al. "HiggsBounds-4: improved tests of extended Higgs sectors against exclusion bounds from LEP, the Tevatron and the LHC". In: *The European Physical Journal C* 74.3 (Mar. 2014). DOI: 10.1140/epjc/s10052-013-2693-2. URL: https://doi.org/10.1140%2Fepjc%2Fs10052-013-2693-2.

[63] Philip Bechtle et al. "HiggsSignals: Confronting arbitrary Higgs sectors with measurements at the Tevatron and the LHC". In: *The European Physical Journal C* 74.2 (Feb. 2014). DOI: 10.1140/epjc/s10052-013-2711-4. URL: https://doi.org/10.1140%2Fepjc%2Fs10052-013-2711-4.

[64] Philip Bechtle et al. "Probing the Standard Model with Higgs signal rates from the Tevatron, the LHC and a future ILC". In: *Journal of High Energy Physics* 2014.11 (Nov. 2014). DOI: 10.1007/jhep11(2014)039. URL: https://doi.org/10.1007%2Fjhep11%282014%29039.

[65] Wolfram Research Inc. *Mathematica, Version 12.0.* Champaign, IL, 2019.

[66] Thomas Hahn. "Generating Feynman diagrams and amplitudes with FeynArts 3". In: *Computer Physics Communications* 140.3 (2001), pp. 418–431. ISSN: 0010-4655. DOI: https://doi.org/10.1016/S0010-4655(01)00290-9. URL: https://www.sciencedirect.com/science/article/pii/S0010465501002909.

[67] Adam Alloul et al. "FeynRules 2.0 — A complete toolbox for tree-level phenomenology". In: *Computer Physics Communications* 185.8 (Aug. 2014), pp. 2250–2300. DOI: 10.1016/j.cpc.2014.04.012. URL: https://doi.org/10.1016%2Fj.cpc.2014.04.012.

[68] R. Mertig, M. Böhm, and A. Denner. "Feyn Calc - Computer-algebraic calculation of Feynman amplitudes". In: *Computer Physics Communications* 64.3 (1991), pp. 345–359. ISSN: 0010-4655. DOI: https://doi.org/10.1016/0010-4655(91)90130-D. URL: https://www.sciencedirect.com/science/article/pii/001046559190130D.

[69] R. L. Workman et al. "Review of Particle Physics". In: *PTEP* 2022 (2022), p. 083C01. DOI: 10.1093/ptep/ptac097.

[70] Michael Spira. In: *Fortschritte der Physik* 46.3 (Apr. 1998), pp. 203–284. DOI: 10.1002/(sici)1521-3978(199804)46:3<203::aid-prop203>3.0.co;2-4. URL: https://doi.org/10.1002%2F%28sici%291521-3978%28199804%2946%3A3%3C203%3A%3Aaid-prop203%3E3.0.co%3B2-4.

[71] *Measurement of the properties of Higgs boson production at* $\sqrt{s} = 13$ *TeV in the* $H \rightarrow \gamma\gamma$ *channel using* 139 fb^{-1} *of pp collision data with the ATLAS experiment.* Tech. rep. 78 pages in total, 25 figures, 20 tables, submitted to JHEP. All figures including auxiliary figures are available at https://atlas.web.cern.ch/Atlas/GROUPS/PHYSICS/PAPERS/HIGG-2020-16. Geneva: CERN, 2022. arXiv: 2207.00348. URL: http://cds.cern.ch/record/2814435.

[72] "A portrait of the Higgs boson by the CMS experiment ten years after the discovery". In: *Nature* (2022). All the figures and tables can be found at http://cms-results.web.cern.ch/cms-results/public-results/publications/HIG-22-001 (CMS Public Pages). DOI: 10.1038/s41586-022-04892-x. arXiv: 2207.00043. URL: http://cds.cern.ch/record/2814513.